



1 **Hidden vortices: Near-equatorial low-oxygen extremes**
2 **driven by high-baroclinic-mode vortices**

3
4 Florian Schütte^{1,2}, Johannes Hahn³, Ivy Frenger¹,
5 Arne Bendinger⁴, Fehmi Dilmahamod¹, Marco Schulz¹, Peter Brandt^{1,2}

6
7 ¹GEOMAR Helmholtz Centre for Ocean Research Kiel, Kiel, Germany

8 ²Christian-Albrechts-University, Kiel, Germany

9 ³Bundesamt für Seeschifffahrt und Hydrographie, Hamburg, Germany

10 ⁴Laboratoire d'Océanographie Physique et Spatiale, University Brest,
11 CNRS, Ifremer, IRD, IUEM, Brest, France

12

13 Corresponding Author: Florian Schütte (fschuette@geomar.de)

14

15

16

17

18 **Keywords:** subsurface low-oxygen/hypoxic patches, high-baroclinic
19 mode vortices, subsurface coherent vortices, submesoscale eddies, low-
20 latitudes / tropical / near-equatorial



21 **Abstract**

22 Long-term time series of dissolved oxygen (DO) measurements from the upper 500 m depth
23 of the eastern tropical North Atlantic (ETNA), collected over a period of up to 15 years at three
24 different mooring sites, reveal recurring extreme low-oxygen events lasting for several weeks.
25 Similarly, observations from 15 individual meridional ship sections between 6°N and 12°N
26 along 23°W show DO concentrations far below 60 $\mu\text{mol kg}^{-1}$ in the upper 200 m - significantly
27 lower than the climatological values at this depth ($>80 \mu\text{mol kg}^{-1}$). Two-third of these low-
28 oxygen events could be related with high-baroclinic-mode vortices (HBVs) with their cores
29 located well below the mixed layer. Despite the energetic equatorial circulation and the
30 expected dominance of wave-like structures in the near-equatorial region, these HBVs persist
31 as relatively long-lived and coherent features. Based on moored and shipboard observations
32 from the ETNA, and supported by an eddy-resolving ocean-biogeochemistry model, we
33 characterize their dynamics and DO distribution. Observed water mass properties and model
34 analyses suggest that most HBVs originate from the eastern boundary and can persist for
35 more than six months. As they propagate westward into regions of higher potential vorticity
36 (PV), anticyclonic HBVs with low-PV cores remain more effectively isolated and have longer
37 lifespans compared to cyclonic HBVs with high-PV core. The vertical structure of the dominant
38 anticyclonic HBVs corresponds to baroclinic modes 4-10, with associated Rossby radii ranging
39 from 34 km to 13 km, respectively. This is consistent with observed eddy sizes and is well
40 below the corresponding 1st baroclinic Rossby radius of deformation ($> 100 \text{ km}$). Since none
41 of the observed HBVs exhibit a surface signature, a substantial portion of the near-equatorial
42 eddy field may remain undetected by satellites, yet still exert significant influence on ocean
43 ecosystems and biogeochemical cycles.



44 1. Introduction

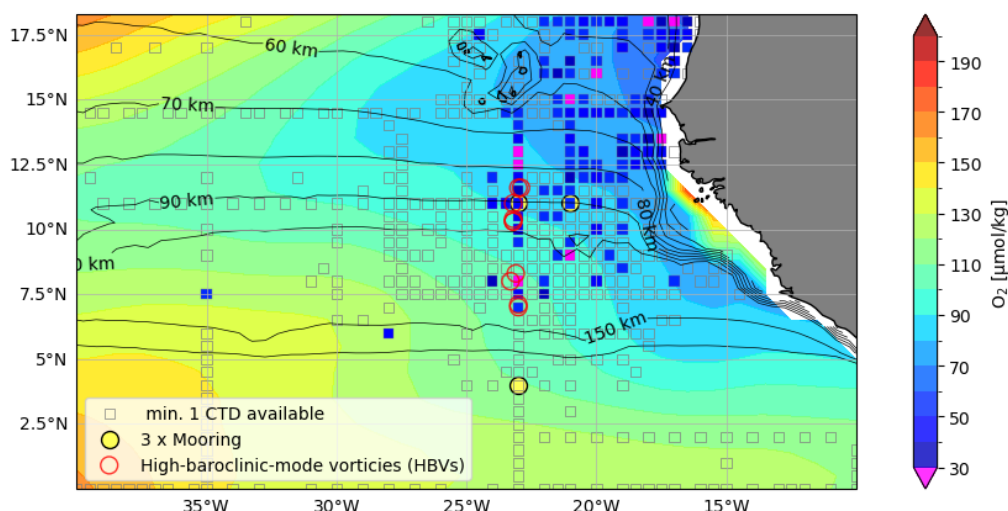
45 Dissolved oxygen (DO) concentration is a key component of marine ecosystems, shaping
46 biodiversity, biogeochemical cycles, and the survival of pelagic species. From long-term
47 moored observations in the open Eastern Tropical North Atlantic (ETNA) near the equator
48 (latitudes $<12^{\circ}\text{N}$), we repeatedly observe short-lived extreme low-oxygen events in the
49 subsurface, well below the mixed layer. This DO variability is likely driven by small-scale
50 vortices, which is unexpected, as theory suggests that wave-like structures should dominate
51 at these latitudes (Eden, 2007). In this study, we combine moored time series, repeated ship
52 transects, and an eddy-resolving biogeochemical model to investigate these small-scale
53 processes below the mixed layer in the tropical Atlantic. This integrated approach allows us to
54 characterize their structure, variability, and strong influence on DO distribution, with potential
55 implications for marine ecosystems and biogeochemical cycles.

56 Extreme events of low DO in isolated cores of large coherent mesoscale eddies have become
57 a well-studied phenomenon of the Atlantic and Pacific eastern boundary upwelling systems
58 (e.g. Stramma et al. (2013); Karstensen et al. (2015); Schütte et al. (2016b); Frenger et al.
59 (2018)). A strong isolation and the longevity of the eddy for at least several months favor a DO
60 depleted eddy core. The DO depleted core results from (i) trapped water, which is transported
61 westward within the eddy core from a region of initially low DO, typically from the eastern
62 boundary (dynamic effect) and (ii) enhanced DO consumption (production effect) due to a
63 biologically high productive regime above the eddy core (McGillicuddy, 2016). The latter is
64 associated with high phytoplankton productivity, which leads to enhanced respiration and
65 reduction of DO beneath the mixed layer directly in the isolated core reaching down to about
66 200 m (Karstensen et al., 2017). Respiration rates in the eddy's interior were found to be
67 substantially increased, with 3 to 5 times the values of ambient conditions for the tropical North
68 Atlantic, e.g. subsurface intensified anticyclonic eddies (subsurface ACEs): $0.19 \pm$
69 $0.08 \mu\text{mol kg}^{-1} \text{ d}^{-1}$ and surface intensified cyclonic eddies (CEs): $0.10 \pm 0.12 \mu\text{mol kg}^{-1} \text{ d}^{-1}$
70 (Schütte et al., 2016b). The increased respiration within these isolated mesoscale eddies may
71 result in anoxic conditions ($< 5 \mu\text{mol kg}^{-1}$) in the otherwise hypoxic ($60 \mu\text{mol kg}^{-1}$) ETNA. Such
72 eddies have a severe impact on biogeochemical processes and organisms (Fiedler et al.,
73 2016; Hauss et al., 2016; Löscher et al., 2015). Moreover, it is suggested that the increased
74 DO consumption within the isolated mesoscale eddy cores promote the formation and
75 existence of a broad-scale shallow DO minimum zone (sOMZ) at about 80 m (Schütte et al.,
76 2016b), that is most pronounced off the nutrient-rich Mauritanian upwelling system in the
77 ETNA, located between 15° and 23°N (Karstensen et al., 2008; Brandt et al., 2015) (Fig. 1).
78 For such low DO extremes to develop highly isolated eddies must form and propagate over a
79 relatively long period through regions of relatively low dynamical activity, e.g. as stated in the



80 mentioned literature north of 12°N in the eastern Atlantic and Pacific oceans.

81 The occurrence of DO depleted long-lived coherent eddies in near-equatorial waters (< 12°) is
 82 not intuitive and contrasts theoretical considerations of equatorial dynamics, which suggest a
 83 dominance of anisotropic wave like structures (Eden, 2007). However, several extreme low DO
 84 events have been observed in the ETNA at latitudes between 6° and 12°N (Brandt et al. 2015),
 85 where Christiansen et al. (2018) associated one of these events (at 8°N, 23°W) with a
 86 subsurface ACE. These eddies are expected to be less isolated and shorter-lived compared
 87 to eddies poleward of these low latitudes. The first baroclinic Rossby radius of deformation
 88 ($R_{d,1}$), which is a characteristic threshold size of a dynamical regime to be in a geostrophic
 89 balance on meso- and larger scales, strongly increases towards the equator (Chelton et al.,
 90 1998). Global eddy studies, mainly based on altimeter sea surface height data, show a strong
 91 equatorward decrease of long-lived (> 35 days) eddies (Chaigneau et al., 2009; Chelton et al.,
 92 2011). Less isolated eddies more readily entrain DO from surrounding waters, while short-lived
 93 eddies do not persist long enough to substantially deplete DO in their cores. Both factors inhibit
 94 the development of a low DO extreme within eddy cores. Additionally, the equatorial region -
 95 compared to the eastern parts of the oceans north of 12°N - is highly dynamic. It features the
 96 energetic equatorial zonal current system with associated instabilities as well as various wave
 97 phenomena (e.g. Urbano et al. 2006; Pena-Izquierdo et al., 2015; Calil et al., 2023; Köhn et al.
 98 2024). Nevertheless, our observations occasionally reveal DO values significantly below the
 99 climatological value (Fig. 1).



100

101 Figure 1: Map of the eastern tropical North Atlantic. Shaded are minimum DO values in the
 102 upper 200 m of the climatological DO distribution from the World Ocean Atlas 2023. The small
 103 squared boxes indicate regions of 0.5 degree boxes for which at least one CTD station is



104 available. These boxes are colored with their minimum DO concentration in the upper 200m
105 (from multiple CTDs, if available) only if the minimum DO concentration is less than 60 $\mu\text{mol/kg}$.
106 Red circles suggest the occurrence of high-baroclinic mode vortices as analyzed in detail in
107 the manuscript. The yellow points mark the positions of the moorings analyzed in the
108 manuscript. The black contour indicates the first baroclinic Rossby radius of the deformation
109 (in km), calculated from the World Ocean Atlas data, following Chelton et al., (1998).

110

111 While mesoscale eddies of the first baroclinic mode can hardly exist at near-equatorial
112 latitudes, smaller-scale eddies might. In the following, we refer to these smaller eddies, which
113 still exhibit similar dynamics to mesoscale eddies - i.e., they are dominantly in geostrophic
114 balance – as high-baroclinic mode vortices (HBVs). They have radii below the first baroclinic
115 Rossby radius, $R_{d,1}$, and baroclinic modes larger than one (D’Asaro, 1988; McCoy et al., 2020,
116 McWilliams et al 1985, 2016). These HBVs, often referred to in the literature as subsurface or
117 submesoscale coherent vortices, are observed to have isolated cores and can therefore advect
118 tracers (Gula et al., 2019). Due to their small spatial scales and since they often appear at
119 subsurface depth, these eddies are not necessarily detectable from satellite observations
120 (McCoy et al., 2020). HBVs are not typically known to persist for extended durations in near-
121 equatorial waters. However, here we provide evidence that HBVs may serve as a potential
122 mechanism driving the observed low-oxygen extremes at these low latitudes. When linked to
123 biogeochemical anomalies, HBVs can play a crucial role in biogeochemical cycles and marine
124 ecosystems. However, ocean models are often submesoscale-permitting only, such that
125 submesoscale processes are not fully resolved, particularly with increasing distance from the
126 equator. Understanding the frequency and behavior of HBVs is essential for understanding
127 tracer distributions, developing effective parameterizations and improving model accuracy.

128 In this study, we identify the characteristics, origin and temporal evolution of low-oxygen
129 extremes in the upper 200 m of the tropical Atlantic Ocean and discuss the role of HBVs in
130 driving these DO deficient zones. We use a comprehensive data set of in situ moored and
131 shipboard observations combined with an actively eddying ocean-biogeochemistry model
132 (respective data and methods introduced in *section 2* and *3*) in order to investigate the
133 frequency distribution and magnitude of these events (*section 4.1*). We show that the low-
134 oxygen events are by the majority related to subsurface intensified HBVs (*section 4.2*), both
135 anticyclonic and cyclonic. We derive the demography of these structures from an eddy
136 detection algorithm applied to in-situ observations (*section 4.3*) and a vertical baroclinic mode
137 analysis (*section 4.4*). The core water of the HBVs is analysed in *section 4.5* and the origin
138 and temporal evolution of the HBVs based in model simulations is shown in *section 4.6*. We
139 give a detailed discussion in *section 5* and provide a summary in *section 6*.

140



141 **2. Data**

142 Data from moored, shipboard and satellite observations, climatological data as well as the
143 output of an actively eddying ocean-biogeochemistry model from the tropical North Atlantic
144 were used within this study as described in the following.

145 **2.1. Moored observations**

146 Multi-year moored observations from three different locations 11°N, 21°W; 11°N 23°W and 4°N
147 23°W were used in this manuscript (Fig. 1). The mooring at 11°N, 21°W was equipped with
148 DO (AADI Aanderaa optodes of model types 3830 and 4330) and CTD (Conductivity,
149 temperature, depth) sensors (Sea-Bird SBE37 microcats) which were attached next to each
150 other on the mooring cable between 2012 to 2018. Eight of these optode/microcat
151 combinations were installed evenly distributed in the depth range between 100 to 800 m,
152 delivering multi-year time series of temperature, salinity and DO with a temporal resolution of
153 up to 5 min. At 800 m depth, an upward looking Acoustic Doppler Current Profiler (ADCP) was
154 installed to record velocity in the depth range between about 60 and 800 m. During the 2nd
155 deployment period (May 2014 to Sep 2015), no velocity observations were available due to a
156 failure of the ADCP. Before and after a deployment period, optodes and microcats were
157 calibrated against CTD-O measurements during CTD casts and onboard lab measurements
158 as described in Hahn et al. (2014) and Hahn et al. (2017). The correction against reference
159 measurements, thereby considering potential sensor drifts (Bittig et al., 2018), allowed best
160 data quality and yielded average root mean square calibration errors of 0.003°C, 0.006 and
161 3 µmol kg⁻¹ for temperature, salinity and DO, respectively. Only quality controlled data that
162 was flagged good was used for further analysis. ADCP measurements were quality controlled
163 against a percent good criterion (20% threshold) and were checked for plausibility and evident
164 outliers due to surface reflection. ADCP bin depths were corrected using a mean sound speed
165 profile following the approach by Shcherbina et al. (2005). This mooring is used to study
166 hydrographic, DO and velocity temporal variability (on daily to intraseasonal time scales)
167 related to low-oxygen extreme events. The other moorings at 11°N 23°W and 4°N 23°W are
168 part of the prediction and research moored array in the tropical Atlantic (PIRATA), which were
169 equipped with DO (AADI Aanderaa optodes of model types 3830 and 4330) sensors at 300 m
170 and 500 m depth from 2009 to 2024. At 11°N, 23°W additionally an DO sensor at 80 m depth
171 was installed between 2017 to 2024. The DO sensors deliver hourly data and are calibrated
172 and processed in the same way as described above.

173



174 **2.2. Shipboard observations**

175 Hydrographic and DO data was obtained from CTD-O casts, that were carried out during a
176 large number of research cruises to the tropical North Atlantic between 2006 and 2022. In the
177 region 6°-12°N and 30°-18°W, 976 profiles were recorded during 24 cruises mainly covering
178 the upper 1300 m of the water column. Two independently working systems of temperature-
179 conductivity-pressure-oxygen sensors were used, that allowed to identify spurious sensor
180 data. Salinity and DO readings were calibrated against values from water samples, that were
181 taken during the majority of CTD-O profiles of each individual cruise and that were measured
182 onboard with salinometry and Winkler titration, respectively. For a single cruise, data accuracy
183 was generally better than 0.002°C, 0.002 and 2 µmol kg for temperature, salinity and DO,
184 respectively.

185 The majority of research cruises covered the 23°W meridian in the tropical North Atlantic. They
186 captured several low-oxygen extreme events in the latitude range between 6° and 12°N (Fig.
187 1). We made use of these CTD-O observations that were mostly carried out at a meridional
188 resolution of 0.5°, corresponding to 55 km, in order to investigate the spatial distribution of the
189 low oxygen extremes. Horizontal velocity data were additionally acquired continuously along
190 the cruise track with vessel-mounted Acoustic Doppler Current profilers (vmADCPs). The
191 typical vmADCP operating frequency was 75 kHz, where 1-hour averaged data has an
192 accuracy of better than 2-4 cm s⁻¹ (Fischer et al., 2003). During one cruise, a vmADCP system
193 with 150 kHz operating frequency was used and we expanded this data set with data from a
194 lowered ADCP (IADCP), that was attached to the CTD rosette and measured velocity profiles
195 at CTD-O cast positions. Single velocity profiles from IADCP had an accuracy of better than
196 5 cm s⁻¹ (Visbeck, 2002). The horizontal velocity observations from all 23°W ship sections
197 covered the depth range of the upper 300 m, the depth where the extreme low-oxygen occur
198 and thus coinciding with our target depth range.

199 For each 23°W ship section hydrography, DO and velocity were mapped onto a regular depth-
200 latitude grid (resolution of 10 m and 0.05°) using a Gaussian interpolation scheme with vertical
201 and horizontal influence (cutoff) radii of 10 m (20 m) and 0.05° (0.1°), respectively (for details
202 see Brandt et al. (2010). This is done to plot the average section along 23°W in order to
203 compare it with the model data and assess the model performance.

204 **2.3. Satellite observations**

205 Sea level anomaly (SLA) and surface geostrophic velocity derived from satellite altimetry
206 products were used in this study to identify the surface signatures of eddies. The multimission
207 Data Unification and Altimeter Combination System (DUACS) product in delayed time and



208 daily resolution with all satellite missions available at a given time is used. It has a spatial
209 resolution of 0.25° and is provided by Marine Copernicus ([https://doi.org/10.48670/moi-](https://doi.org/10.48670/moi-00148)
210 00148).

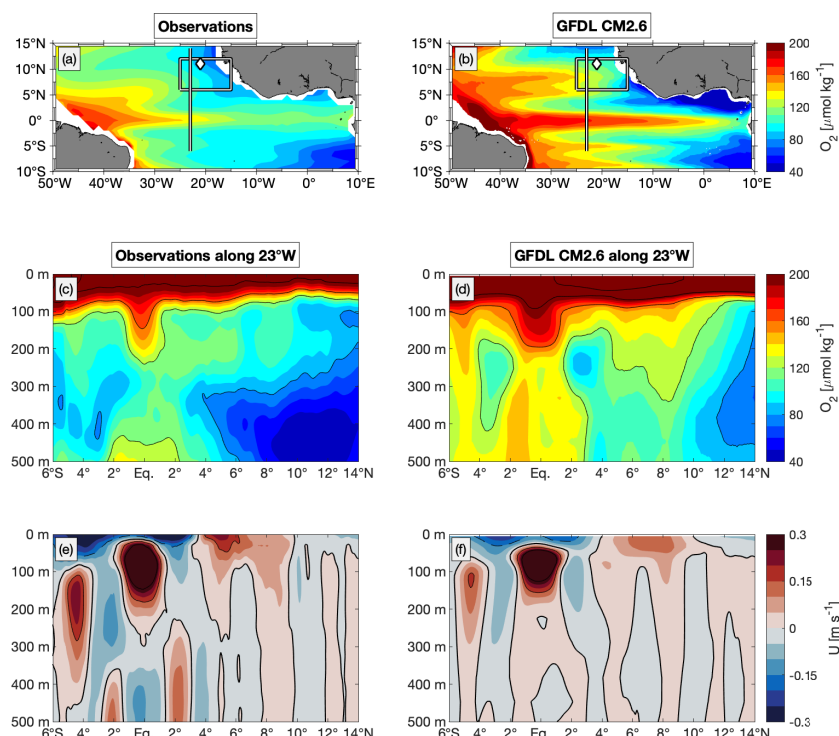
211 **2.4. Climatological data**

212 Gridded climatological hydrography and DO from the World Ocean Atlas 2023 (WOA23)
213 (described e.g. in Reagan et al. 2024) was used as a reference data set throughout this study.
214 In addition, the monthly, isopycnal and mixed-layer ocean climatology (MIMOC) (Schmidt et
215 al., 2013) was used. For more details see section 6 *Data availability*.

216 **2.5. Coupled ocean-biogeochemistry model**

217 We used the output of the GFDL climate model with an eddy-rich ocean, CM2.6 (Delworth et
218 al., 2012; Griffies et al., 2015) to further understand the origin and development of low-oxygen
219 extremes in the tropical ocean. CM2.6 has a nominal ocean resolution of 0.1 degrees and an
220 atmosphere with approximately 50 km resolution. For computational efficiency, marine
221 biogeochemistry is represented by the simple biogeochemical model MiniBLING (Galbraith et
222 al., 2015). MiniBLING was run with the three prognostic tracers dissolved inorganic carbon,
223 phosphate and DO. Organic carbon (biomass) is treated diagnostically and is not advected in
224 the model. Despite its simplicity, MiniBLING has been shown to perform comparably well to
225 more complex marine biogeochemical models in simulating marine biogeochemistry and its
226 sensitivity to climate (Galbraith et al., 2015). Moreover, the small number of tracers was not
227 just a limitation but a key factor that made it possible to run a simulation with a mesoscale-rich
228 ocean.

229 The results we show here stem from a simulation with preindustrial atmospheric carbon dioxide
230 levels that has been run for 200 years, with marine biogeochemistry coupled at year 48. The
231 model has been spun up from rest with initial conditions from WOA09 (Locarnini et al., 2010;
232 Antonov et al., 2010; Garcia et al., 2010a; Garcia et al., 2010b) and Global Ocean Data
233 Analysis Project (GLODAP) (Key et al., 2004). For more details on the model set up and a
234 general evaluation of the model we refer to Griffies et al. (2015) and Dufour et al. (2015). Here,
235 we used five daily model outputs of the last 20 years of the simulation. A brief evaluation of the
236 model performance for the northern hemispheric Atlantic DO conditions, the focus of our study,
237 is given in the following.



238

239 Figure 2: Observation-model comparison of the minimum DO between 0 and 200 m of the
 240 time-average distribution from (a) MIMOC and (b) from last 20 years of GFDL CM2.6 model.
 241 Latitude-depth section, 0-500 m along 23°W, of mean DO from (c) repeat ship sections and
 242 (d) last 20 years of GFDL CM2.6 model. (e) and (f) are similar to (c) and (d), but mean zonal
 243 velocity is shown. The box in (a) and (b) illustrates the area of interest in this study; the line
 244 denotes the 23°W section that is shown in subpanels (c) to (f). This section has been surveyed
 245 by 15 individual shipboard observations that are used in this study for the latitude range 6°N-
 246 12°N. Diamond marks the mooring position (21°W, 11°N), where data used in this study were
 247 taken.

248 The distribution of the minimum DO between 0 and 200 m taken from the time averaged over
 249 the last 20 years of the GFDL CM2.6 model output (Fig. 2b), shows similar large-scale patterns
 250 as the same corresponding distribution taken from the MIMOC climatology (Fig. 2a): well
 251 oxygenated western boundary region, decreasing DO values toward east with off-equatorial
 252 OMZs on both sides of the equator showing minimal values at the eastern boundary. The
 253 simulated distribution has higher DO concentration at the western boundary and in the interior
 254 basin, and partly lower values at the eastern boundary compared to the climatological
 255 distribution from observations, which is particularly the case in the Gulf of Guinea region. In
 256 the interior basin, meridionally alternating bands of oxygen-poor and oxygen-rich water, that
 257 are associated with shallow east- and westward current bands, are pronounced in GFDL
 258 CM2.6, albeit more intensified.



259 In the ETNA, the average DO distribution along 23°W in GFDL CM2.6 (Fig. 2d) shows a
260 notable mismatch with observations (Fig. 2c). While observations from repeat ship sections
261 reveal two distinct OMZ layers - a shallow OMZ above 200 m and a deeper OMZ at 300 - 700
262 m - the model instead simulates only a single OMZ spanning 100 - 600 m. This bias is also
263 present in other coupled ocean circulation biogeochemistry models (e.g. Duteil et al., 2014).
264 Further differences appear south of the equator, where the observed OMZ is absent in the
265 model along 23°W. Instead, GFDL CM2.6 simulates lower DO levels between 2°- 4°N at
266 depths below 150 m compared to observations. The corresponding section of zonal velocity
267 (Fig. 2f) indicates that the model represents upper-ocean currents (above 200 m) well when
268 compared to observations (Fig. 2e). However, below 200 m in the equatorial region (5°S -5°N),
269 zonal currents are considerably weaker and partly misrepresented. North of 5°N, the velocity
270 structure is generally better captured.

271 Despite differences in spatial details and magnitudes the basic features of the DO and velocity
272 distributions are in the upper 200 m of the ETNA, and the GFDL CM2.6 model provides a
273 robust physical and biogeochemical background state to study the role of eddies in driving
274 local DO deficient zones. The model has been shown to simulate low-oxygen mesoscale
275 eddies at latitudes poleward of about 12° latitude (Frenger et al., 2018). Here, we use the last
276 20 years of this model run to study low-oxygen extreme events in the ETNA equatorward of
277 12°N.

278 **3. Methods**

279 Different diagnostics have been applied in this study, that allowed us to associate low-oxygen
280 features with HBVs and to analyze their origin and temporal evolution. The concept of vertical
281 baroclinic modes (*section 3.1*) was used to characterize the vertical structure of HBVs, to
282 identify the dominant vertical modes, and their associated Rossby radius of deformation and
283 propagation speed. In *section 3.2*, we briefly present the calculation of PV, which is used as a
284 conservative tracer to track and to identify the isolation of different water masses. In *section*
285 *3.3*, we describe the different approaches for eddy identification from shipboard observations
286 and in the GFDL CM2.6 model.

287 **3.1. Vertical baroclinic modes and Rossby radius of deformation**

288 A powerful way to describe linear wave dynamics in the ocean is the decomposition into vertical
289 baroclinic modes (Philander, 1978). Each baroclinic mode is associated with a specific gravity
290 wave speed and a corresponding Rossby radius of deformation, which defines its
291 characteristic horizontal length scale.



292 **3.1.1. Baroclinic mode decomposition**

293 The concept of baroclinic modes is based on the linearized hydrostatic equations of motion,
294 which can be separated into a horizontal and a vertical component. Assuming a motionless
295 background state and a flat-bottomed ocean, the vertical structures are given by solving the
296 eigenvalue problems (Gill, 1982):

$$\frac{d^2 \Psi_n(z)}{dz^2} + \frac{N^2(z)}{c_n^2} \Psi_n(z) = 0 \quad (1)$$

297 where $\Psi_n(z)$ describes the vertical structures of isopycnal displacement ξ or vertical velocity
298 w and z is the vertical coordinate. $N(z)$ is the vertical profile of the Brunt-Väisälä frequency
299 and c_n the gravity wave speed for mode $n \in \mathbb{N}$. For the eigenvalue problem (1), we use
300 boundary conditions with a free surface and a flat bottom (Gill, 1982), which are given as

301

$$\Psi_n = \frac{c_n^2}{g} \frac{d\Psi_n}{dz}, \text{ at } z = 0 \quad \text{and} \quad \Psi_n = 0, \text{ at } z = -H \quad (2)$$

302 where H is the ocean depth and g the gravitational acceleration. For a continuously stratified
303 ocean, the number of solutions depends on the vertical resolution of the data used. Any
304 perturbances can be described as a superposition of orthogonal vertical baroclinic modes ($n =$
305 1, 2, 3, ...). Amplitudes of vertical structure functions are normalized such that

$$\int_{-H}^0 \Psi_n \Psi_m dz = \delta_{nm} H \quad (3)$$

307 where δ_{nm} is the Kronecker delta and n, m the modes. The gravity wave speed is related to
308 the Rossby radius of deformation, that can be calculated for the off-equatorial regions
309 (poleward of 5°S and 5°N) as

310

$$R_{d,n} = \frac{c_n}{|f|} \quad (3)$$

311 (Gill, 1982 or Chelton, 1998), where $R_{d,n}$ is the Rossby radius of deformation for the n -th
312 vertical baroclinic mode, and f is the Coriolis parameter.



3.1.2. Calculation of vertical baroclinic modes and modal decomposition

The main goal is to decompose any disturbed state into the set of orthogonal baroclinic modes that solve (1). Each hydrographic profile from an individual CTD-O profile can be considered as a perturbation from the mean state. The mean state distribution was derived from the 3-D climatological hydrographic field (cf. Chelton et al. (1998)) that is given by the World Ocean Atlas (*section 2.4*). Given the corresponding density profile, we calculated the isopycnal displacement $\xi(z)$ by

$$\xi(z) = \frac{\rho'(z) \cdot g}{\rho_0 \cdot N^2} \quad (4)$$

with $\rho'(z) = \rho(z) - \rho_{ref}(z)$, $\rho_0 = 1025 \text{ kg/m}^3$ a constant reference density and ρ_{ref} being the undisturbed profile of potential density (here taken as the climatological density profile from the World Ocean Atlas – see also Vic et al. 2021 for more details on the method used). The isopycnal displacement of the disturbed state can be described as a superposition of the orthogonal set of vertical baroclinic modes for displacement, i.e.

$$\xi(z) = \sum_{n=1}^K x_n \psi_n(z) \quad (5)$$

Here, $K \rightarrow \infty$ expresses the exact solution with an infinite number of vertical modes for a continuously stratified ocean. The expansion coefficients x_n are the modal amplitudes. The modal amplitudes are obtained by projecting the observed fields onto the structure functions computed from the World Ocean Atlas. The projection is preferred over resolving a least-square problem, which sometimes leads to unrealistic modal amplitudes into the high modes (Vic et al. 2023). The modal amplitudes x_n are calculated via a scalar product:

$$x_n = \int_{-980}^{-30} \psi_n(z) \cdot \zeta_{CTD}(z) dz \quad (6)$$

These amplitudes are then normalized by dividing with $\int_{-980}^{-30} \psi_n(z)^2 dz$. This analysis is restricted to the depth range from 30 m to 980 m in order to exclude the surface mixed layer while retaining the majority of available profiles along 23°W. The barotropic mode assumed to be zero. A vertical resolution of 10 m is used, with both the CTD profiles and World Ocean Atlas data interpolated accordingly. After computing the contribution of one mode, it is subtracted from the displacement profile: $\xi'(z) = \xi(z) - x_n \psi_n(z)$ and the procedure is



338 repeated for the next mode. This recursive removal reduces cross-talk between modes caused
339 by the limited vertical resolution and incomplete depth coverage. Since the order of mode
340 extraction may influence the result, the decomposition is repeated $M = 100$ times with random
341 permutations of modes $n = 1$ to $n = 20$, and the final modal amplitudes are calculated as the
342 mean over all realizations, with associated standard errors.

343 **3.2. Potential vorticity and Rossby number**

344 Subsurface eddies exhibit signatures of high or low potential vorticity (PV), depending on their
345 stratification anomaly and rotation direction (D'Asaro, 1988; McWilliams, 1985; Molemaker et
346 al., 2015). In the absence of mixing, PV is a conserved quantity and serves as an effective
347 tracer to differentiate water masses and track eddy pathways.

348 We refer to Ertels PV (Gill, 1982), being one of the most complete formulations for PV
349 conservation, and take its vertical approximation (see e.g. Thomsen et al. (2016)), which is
350 given by

$$Q = (\zeta_z + f) \cdot N^2 \quad (7)$$

351 where $\zeta_z = \frac{\partial v}{\partial x} - \frac{\partial u}{\partial y}$ is the vertical component of the relative vorticity and f is the Coriolis
352 parameter. The term $\zeta_z + f$ represents the absolute vorticity. The approximation given by (7)
353 is valid in case of nearly horizontally orientated isopycnal surfaces (Thomsen et al. 2016).
354 Counter-clockwise and clockwise rotating eddies correspond to positive and negative relative
355 vorticity, respectively. In the northern hemisphere, anticyclonic eddies rotate clockwise and
356 have negative relative vorticity (vice versa for the southern hemisphere, which is not further
357 considered throughout this study).

358 In the case of geostrophic balance, the Rossby number

$$Ro = \frac{U}{Lf} = \left| \frac{\zeta_z}{f} \right| \quad (8)$$

359 where U is characteristic velocity and L is characteristic length scale, is smaller than one and
360 PV is always positive. PV can be reduced by either a reduction of N^2 (weakened stratification)
361 or by a gain of anticyclonic relative vorticity (D'Asaro, 1988). The explanation also applies vice
362 versa, i.e. PV can be increased by a strengthening in stratification or a gain of cyclonic relative



363 vorticity. The Rossby number becomes larger than one for submesoscale dynamics in the
364 ageostrophic range.

365 **3.3. Eddy identification algorithms**

366 **3.3.1. Eddy identification from shipboard observations**

367 Horizontal velocity data from the vmADCP system (see *section 2.1*) is used to detect eddies
368 along the 23°W meridian between 6°N and 12°N. This methodology is based on an idealized
369 eddy solution, known as Rankine vortex characterized by solid-body rotation in its inner core,
370 i.e., a linear increase of velocity with increasing distance from the eddy center. We do so
371 through the conversion from Cartesian into cylindrical coordinates in areas that are suspected
372 to cross eddies. Every point in the horizontal plane is defined by the radial distance, r , to the
373 origin (eddy center) and the azimuthal angle, θ , i.e.,:

$$374 \quad v_r = u \cos \theta + v \sin \theta \quad (9)$$

$$375 \quad v_\theta = -u \sin \theta + v \cos \theta \quad (10)$$

376 where v_r and v_θ are the radial and azimuthal velocities, respectively. Following Castelao and
377 Johns (2011) and Castelao et al. (2013) the optimal eddy center is found by minimizing v_r
378 (maximizing v_θ) via a non-linear least-squares Gauss-Newton algorithm.

$$379 \quad |v| = -u \sin(\theta) + v \cos(\theta) + \epsilon \quad (11)$$

$$380 \quad \theta = \arctan(y_r / x_r) \quad (12)$$

$$381 \quad y_r = y - y_c \quad (13)$$

$$382 \quad x_r = x - x_c, \quad (14)$$

383 where (x, y) are the position vectors of the velocity samples, and (x_c, y_c) the eddy center
384 location. The residual ϵ represents the radial velocity to be minimized. This methodology
385 assumes a radially axisymmetric and non-translating vortex. The optimal eddy center allows
386 us to determine an azimuthal velocity structure, which in turn provides an estimate for the
387 speed-based eddy radius, i.e. the radius where the azimuthal velocity is maximum while
388 separating the inner core from the outer ring.

389 **3.3.2. Eddy identification in GFDL CM2.6 model**

390 From the GFDL CM2.6 model, we analyzed the position and trajectory of an individual
391 simulated eddy that was representative in terms of its westward propagation in low latitude



392 waters and its associated DO minimum. The horizontal eddy center at each model time step
393 was identified by locating the maximum of the streamfunction within a predefined $3^\circ \times 3^\circ$
394 longitude-latitude box centered on the eddy on a defined isopycnal surface. Once the position
395 was found, we searched for the DO minimum around the eddy center within a $0.8^\circ \times 0.8^\circ$
396 horizontal box. On average, the deviation between the two positions was about 20 km.
397 Additionally, for each time step, we extracted the following variables: DO and salinity on
398 isopycnal surface 26.5 kg m^{-3} , PV on the isopycnal surface 26.6 kg m^{-3} (corresponding to the
399 isopycnal layer of minimum PV, see Fig. 4m), phosphate, and biomass integrated over the top
400 100 m, and particulate organic phosphorus at 100 m (to identify the downward flux of organic
401 matter to the eddy core). To assess eddy anomalies, we compared these variables to their
402 corresponding values outside the eddy (average over the area 1° to 3° longitude/latitude away
403 from the eddy core), and also calculated the 20-year model mean at the eddy core position.

404 Around the eddy position, we identified the streamline with the strongest swirl velocity and
405 calculated the eddy radius $R = \frac{A}{2\pi i}$, assuming an isotropic circular eddy, where A is the
406 circumferences (length of contour). The swirl velocity U was calculated as the average of the
407 absolute value of the horizontal velocity along this contour. The propagation speed c was
408 derived from the horizontal distance between adjacent eddy core positions (as determined by
409 the streamfunction criterion). To assess the isolative character of the eddy, we calculated the
410 isolation parameter U/c , where values greater than 1 indicate isolation of the eddy core water
411 from surrounding water masses.

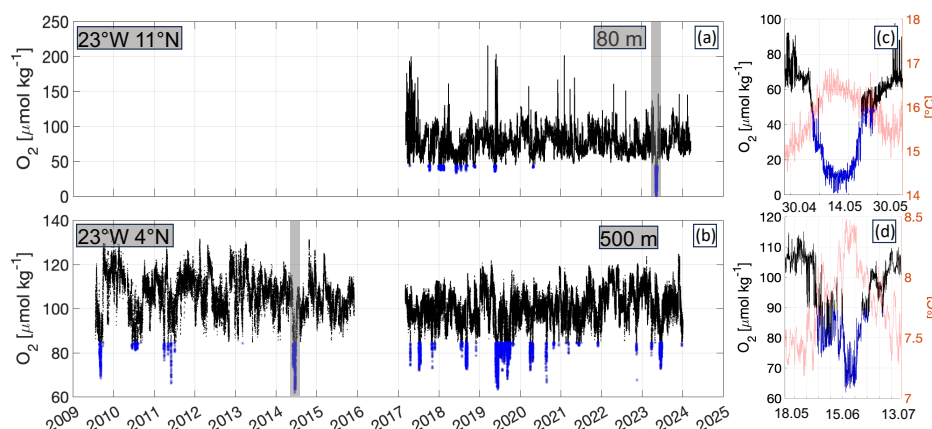
412 4. Results

413 4.1. Near-equatorial low-oxygen events: Frequency, magnitude and duration

414 In all depth of the long-term DO time series from moored observations at 4°N and 11°N (both
415 at 23°W), recurring dips in DO levels are observed that fall significantly below the climatological
416 mean (Fig. 3 a, b). A low-DO extreme event is defined when DO values drop below the 10th
417 percentile of the respective time series. These events typically last from several days to a few
418 weeks and stand out clearly in the time series. They are often accompanied by a temperature
419 increase (Fig. 3c, d). On average, around two such events per year are observed at 4°N at
420 both 300 m and 500 m depth. At 11°N , about one event per year is seen at those depths, and
421 approximately two per year at 80 m. A similar pattern is found in the moored time series from
422 11°N , 21°W , where ten low-oxygen events ($40\text{--}60 \mu\text{mol kg}^{-1}$) were recorded between 2012
423 and 2018 in the upper 200 m. Each event lasted about 3 - 4 weeks.



424 As expected, is the DO variability and amplitude in general higher at shallower depths (e.g. 80
425 m), driven by stronger near-surface dynamics and the higher background DO concentrations.
426 Therefore the largest DO drops were typically observed at 80 - 100 m. In terms of spatial
427 variability, we see that the DO variability within the core of the deep oxygen minimum zone
428 (OMZ) at 11°N is generally lower than at 4°N.

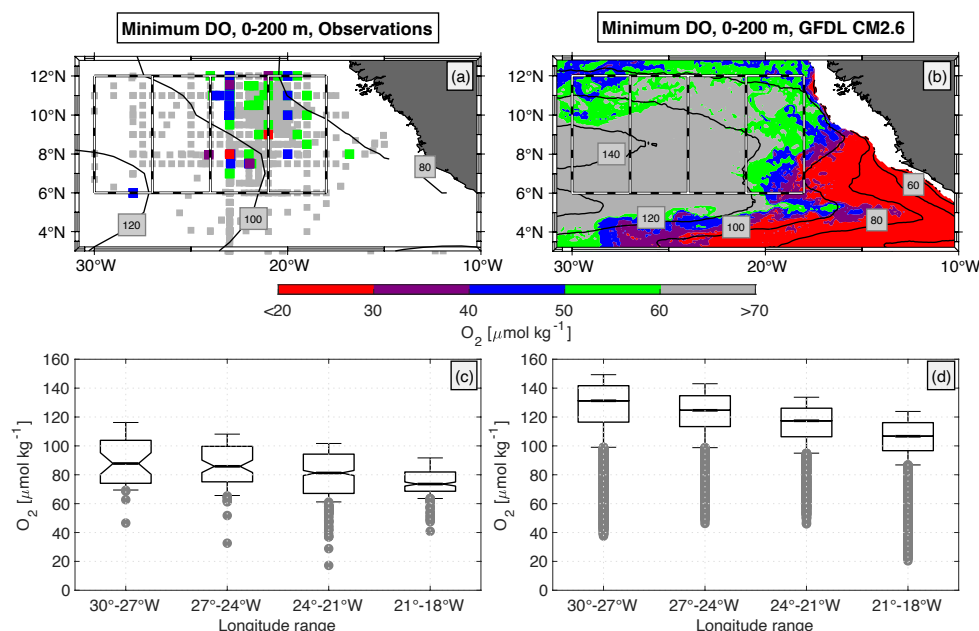


429
430 Figure 3: Time series of observed DO at (a) 80m depth at 23°W, 11°N and 500 m depth at
431 23°W, 4°N shown in black. The blue color represent the lowest 10th percentile of the time
432 series data. The grey boxes mark the timespan which is shown in (c) and (d), where the
433 temperature is overlaid in red.

434 In addition to the moored DO observations, there are multiple years of shipboard
435 measurements in the region. From all these shipboard observations, low-DO extremes are
436 identified by searching for the minimum DO concentration in the upper 200 m of every single
437 CTD-O profile. A low-DO extreme event was defined when DO was below a threshold of
438 $60 \mu\text{mol kg}^{-1}$, which represents the 10-percentile of all DO observations (74 of 976) in the area
439 $6^{\circ}\text{-}12^{\circ}\text{N}$, $30^{\circ}\text{-}18^{\circ}\text{W}$ (Fig. 4a and 4c). This threshold is more than $20 \mu\text{mol kg}^{-1}$ below the
440 climatological DO concentration in the ETNA (Fig. 2a and 2b). Considering the absolute DO
441 concentration allowed us to derive a distribution of low-oxygen extremes, which is not masked
442 by the mean distribution. Lowest DO concentrations below $40 \mu\text{mol kg}^{-1}$ (7 of 976 CTD-O
443 profiles) in the near equatorial region (south of 12°N) remarkably occurred not east of 21°W ,
444 where profiles are located within a distance of 8° to the African coast, but in the “open-ocean”
445 region west of it ($24^{\circ}\text{-}21^{\circ}\text{W}$) (Fig. 4a). Further to the west ($>24^{\circ}\text{W}$), lowest DO concentrations
446 were found again just above $40 \mu\text{mol kg}^{-1}$. This is in contrast to the more coastal upwelling
447 region north of 12°N , where very low-DO extremes can also be observed near the coast (see
448 Fig. 1 or Schütte et al. 2016b). In order to scale for the different number of CTD-O profiles in



the four regions shown in Fig. 4a (5%, 9%, 61% and 25% of the profiles for the boxes 30°-27°W, 27°-24°W, 24°-21°W, 21°-18°W), we estimated the relative distribution and calculated the 10-percentile threshold in every box (Fig. 4c). This threshold is lowest in the open ocean (24°-21°W), whereas the mean DO distribution is increasing from the eastern boundary towards west. This counterintuitive distribution of low-oxygen extremes, which is against the mean DO gradient, suggests that DO depleted water generally cannot be purely advected from a remote region at the eastern boundary, that is poor in DO. Locally enhanced biological activity associated with enhanced DO consumption must play a role as well.



457

Figure 4: (a) Spatial distribution of DO profiles acquired from shipboard CTD-O observations in the tropical North Atlantic. Colored / gray dots denote DO profiles with a minimum DO concentration of lower / higher than 60 $\mu\text{mol kg}^{-1}$ in the depth range 0-200 m (red: < 30 $\mu\text{mol kg}^{-1}$, violet: 30-40 $\mu\text{mol kg}^{-1}$, blue: < 40-50 $\mu\text{mol kg}^{-1}$, green: < 50-60 $\mu\text{mol kg}^{-1}$). (b) Horizontal distribution of DO minimum obtained in the depth range 0-200 m and from the last 20 years of GFDL CM2.6 model run. Black contour lines in (a) and (b) show 0-200 m minimum of mean DO distribution (similar to filled contours in Fig. 2a and 2b). Dashed boxes denote different regions of interest for boxplots shown in (c) and (d). (c) Boxplots for 0-200 m minimum of DO profiles, that are shown for four different regions by the dashed boxes in (a). Thick line in each boxplot denotes median and notches show 95% confidence interval. Upper and lower whiskers denote 10% and 90% quantiles. Grey dots below the lower whiskers show 10% lowest DO events. (d) Similar to (c), but boxplots shown for 0-200 m minimum of DO profiles that were taken from the last 20 years of GFDL CM2.6 model run



471 The two events with the lowest dissolved oxygen (DO) concentrations were measured as 17
472 $\mu\text{mol kg}^{-1}$ by a CTD at 60 m depth at 8°N, 23°W, while concentrations even below 5 $\mu\text{mol kg}^{-1}$
473 were recorded by a mooring at 80 m depth at 11°N, 23°W. These two low-oxygen extremes
474 were well below the climatological average minimum DO concentration for the whole ETNA
475 (40 $\mu\text{mol kg}^{-1}$ in the deep OMZ, Brandt et al. (2015)). We shall note, that no CTD-O profiles
476 were available in this data set for the eastern boundary region within about 2° longitude off the
477 African coast.

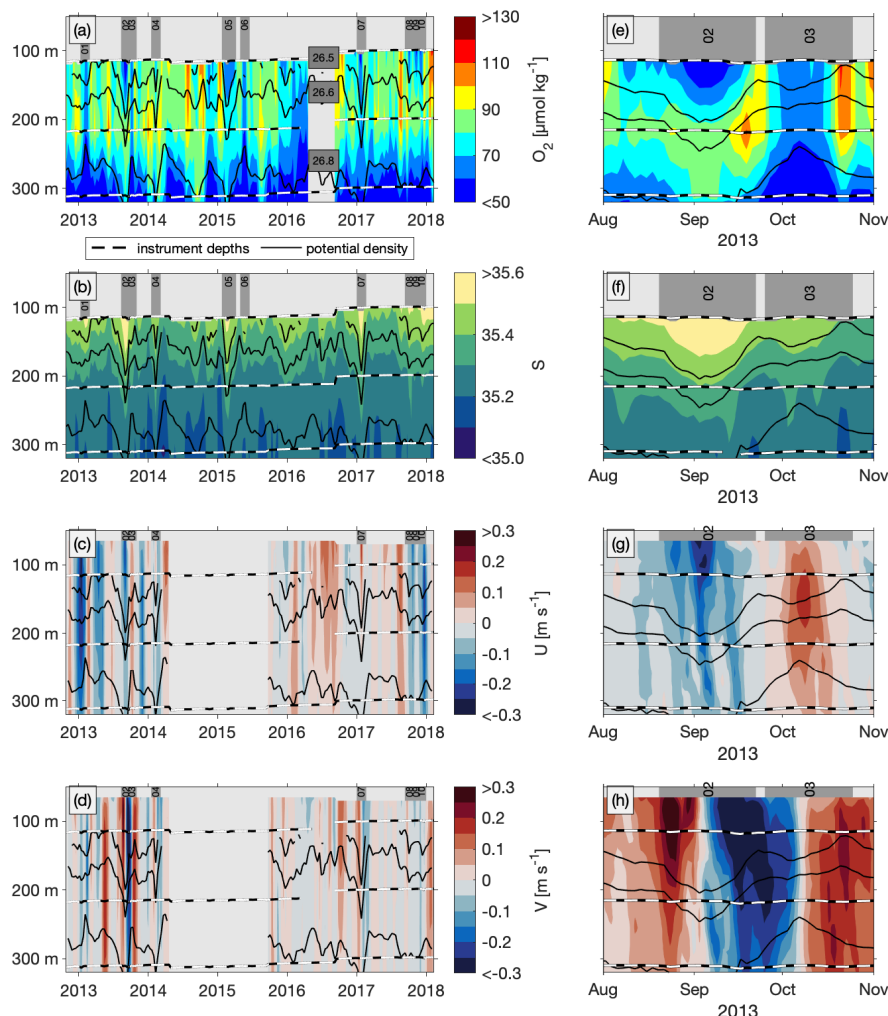
478 **4.2 Association of low-oxygen events with subsurface high-baroclinic mode** 479 **vortices**

480 For the majority of the ship based data and for the mooring at 21°W, 11°N additional
481 observations of hydrography, zonal and meridional velocity are available indicating the
482 passage of anticyclonically and cyclonically rotating vortices associated to the low-oxygen
483 events. At the mooring position the low-oxygen events #01, #02, #03, #04 and #07 were most
484 likely related to the passage of subsurface intensified vortices, whereof events #02, #04 and
485 #07 were associated with anticyclonic vortices and events #01 and #03 with cyclonic vortices
486 (Fig. 5). Note, that we explicitly refer here to the notation *vortex*, since we could not derive the
487 vortices' radii in order to differentiate between mesoscale and submesoscale. For the
488 anticyclonic vortices, meridional velocity was observed with maximum northward and
489 southward flow taking place at the beginning and the end of each low-DO period. Zero crossing
490 was observed in between at around the time, when DO was at its minimum (Fig. 5e to 5h).
491 Corresponding time series of potential density derived from hydrographic observations,
492 conducted next to the DO sensors, indicated a depression of isopycnal surfaces in the depth
493 range below 100 m. Time series of velocity and potential density agree well with the dynamical
494 understanding and passage of westward propagating eddies (van Leeuwen, 2007) through the
495 mooring site. Zonal velocity was either small or showed maximum flow during time periods of
496 minimum DO, depending whether the eddy has crossed the mooring site either with its core or
497 with one of its meridional flanks. Zonal velocity vanished at the beginning and the end of each
498 of the three events.

499 During events #01 and #03, that are associated with the passage of subsurface intensified
500 cyclonic vortices, we found a depression of isopycnal surfaces above 150 m and a heave of
501 isopycnal surfaces below ((cf. McGillicuddy (2015), denoted as eddies of type Thinny). This is
502 associated with a maximum in stratification at about 150 m depth. The time series of zonal and
503 meridional velocity, respectively, showed maximum values at a similar depth with a transition
504 from westward to eastward (event #01) and southward to northward (event #03) velocities



505 during the time of maximum stratification. In contrast to the anticyclonic vortex events (#02,
506 #04 and #07), the DO minima during the passage of the two cyclonic vortex events (#01 and
507 #03) were of similar intensity at 100 and 200 m depth, with no separation from the deep OMZ
508 at 300 m by an intermediate DO maximum. Though, during both events the minimum DO at
509 100 m was well below the average DO concentration that was observed for time periods
510 without any vortex event. We shall explicitly note, that the characteristics for zonal and
511 meridional velocity during event #01 were swapped compared to the other eddy events (#02,
512 #03, #04 and #07). We can only speculate whether this cyclonic vortex has crossed the
513 mooring site in a more meridionally directed pathway.



514 Figure 5: Time series of observed (a) DO, (b) salinity, (c) eastward and (d) northward velocity
515 from moored observations at 11°N, 21°W in the upper 300 m as a 10-day average (color
516 shading). Black lines denote depth of potential density surfaces 26.5, 26.6 and 26.8 kg m^{-3} .
517



518 Black-white dashed lines denote depths of DO sensors (in (a), (c) and (d)) and salinity sensors
519 (in (b)). Gray bars with numbers 01-10 in the top of these panels denote time periods of low-
520 DO events (#01 to #10). Note, that no velocity observations are available for low-DO events
521 #05 and #06. Panels (e)-(h) show corresponding 2-day averaged time series for the 90-day
522 time period around low-DO events #02 and #03.

523 The vertical structure of these vortices could not be identified for the near surface layer and
524 the deep ocean, since moored hydrographic and velocity observations were only available
525 between 100 m (60 m for velocity) and 800 m depth. This made it challenging to distinguish
526 among surface intensified and subsurface intensified (but at shallow depth) vortices. The most
527 likely subsurface intensified vortex was associated with event #02, showing extreme velocity
528 (both zonal and meridional) slightly below the shallowest depth of available observation
529 accompanied by an oxygen minimum of $39 \mu\text{mol kg}^{-1}$.

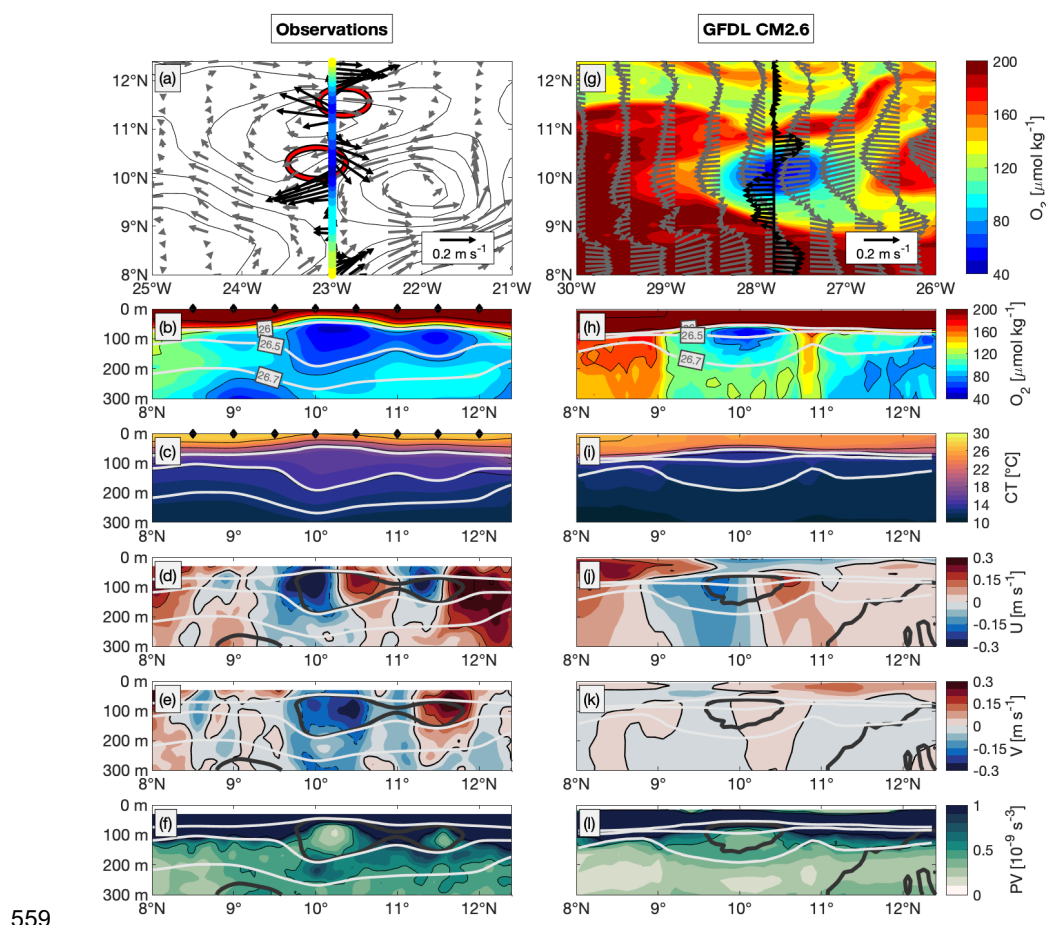
530 **4.3 Horizontal extent of the low-oxygen high-baroclinic mode vortices**

531 The ship-based data, which cover the region spatially, are significantly better suited than the
532 stationary moored data for assessing the spatial extent of the HBVs. Repeated meridional ship
533 sections between $6\text{--}12^\circ\text{N}$ along 23°W , available over a distance of at least 300 km, captured
534 15 events with DO concentrations well below $60 \mu\text{mol kg}^{-1}$ in the upper 200 m (Table 1, Fig.
535 6.). All DO minima were found directly below the shallow oxycline at depths between 45 and
536 90 m (corresponding to surfaces of potential density between $\sigma_\theta = 26.2$ and 26.4 kg m^{-3}). The
537 meridional resolution of CTD-O measurements did not allow for a proper identification of the
538 meridional core position of the low-DO extremes, but their extent was found with roughly 1° in
539 latitude in maximum. The low-DO cores vertically extended to the isopycnal $\sigma_\theta = 26.5 \text{ kg m}^{-3}$
540 (150 m depth) and were separated from the deep OMZ by an intermediate DO maximum
541 located at about $\sigma_\theta = 26.7 \text{ kg m}^{-3}$ (between 200 and 300 m), which rules out a simple vertical
542 displacement of the vertical gradient.

543 We analyzed the distribution of zonal and meridional velocity at the depth of the DO minimum
544 using an eddy identification algorithm as described in *section 3.3.1*. Strikingly, 66% (10 of 15)
545 of the low-DO events could be related to HBVs, where radii were identified between 20 and 45
546 km (average 34 km) (Table 1 Fig. 6b and 6d). The radii are substantially smaller than the typical
547 mesoscale (first baroclinic Rossby radius of deformation) at these latitudes being at the order
548 of 100 km or more. Instead, these eddies have a confined baroclinic structure, which is
549 associated to higher baroclinic modes and corresponding smaller Rossby radii of deformation
550 as is shown in detail in *section 4.4*. The HBVs' horizontal core positions are estimated from the
551 current velocities and closely match the meridional position of the low-oxygen extremes (cf. 3rd



552 and 6th column for bold marked events in Table 1; Fig. 6a and 6b). Note, that the derived HBVs'
553 zonal core position range between 23.3°W and 22.9°W, whereas for the low-oxygen extremes,
554 only the meridional position along the 23°W section can be identified. Notable is the
555 simultaneous occurrence of two HBVs observed during one cruise in 2009 at positions 10.3°N,
556 23.2°W and 11.6°N, 22.9°W (Fig. 6a to 6f). These two HBVs were meridionally cut through
557 their eastern and western flank, respectively, and were both observed with DO concentrations
558 well below 50 $\mu\text{mol kg}^{-1}$ (Fig. 6a and 6b).



560 Figure 6: (a) Current velocity (black arrows) and DO (colored dots) at 80 m depth along 23°W
561 and between 8° and 12°N obtained from along-track shipboard ADCP observations and
562 CTD-O observations between 23-Jul-2009 and 25-Jul-2009 (cruise Ron Brown 2009, see
563 Table 1). Grey arrows show geostrophic velocities and black contours show sea level
564 anomalies from satellite altimetry data on 24-Jul-2009. Red circles denote positions and extent
565 of the two eddies, identified and reconstructed from shipboard ADCP observations at 80 m.
566 Latitude-depth sections of (b) DO, (c) conservative temperature, (d) zonal velocity, (e)
567 meridional velocity and (f) PV between 8° and 12°N obtained from CTD-O observations along
568 23°W (same period to (a)). Black diamonds at the top of panels (b) and (c) denote actual



latitudes of CTD-O profiles. Thin gray lines in panels (b) to (f) denote surfaces of potential density. In panels (d)-(e), solid black and dashed black lines denote 0.15 m s^{-1} velocity intervals. Thick dark gray lines in panels (d)-(f) denote DO contours of $70 \mu\text{mol kg}^{-1}$. (g)-(l) are analog to (a)-(f), but taken from GFDL CM2.6 model simulation for model date 23-Mar-0197. Gray arrows in (g) denote surface velocity. Black arrows denote current velocity and colored contours show DO distribution both at 77 m depth along $\sim 28^\circ\text{W}$. (h) to (l) show respective latitude-depth sections along $\sim 28^\circ\text{W}$ for the same model date. Thick dark gray lines in panels (j)-(l) denote DO contours of $90 \mu\text{mol kg}^{-1}$.

Both HBVs were identified to be anticyclonic and subsurface intensified, as shown by the anomalously weak stratification along 23°W at subsurface depth, which is indicated by the thickening of isothermal and isopycnal layers at the depth range of the DO minimum core (Fig. 6c). The vertical extent of the HBVs (characterized by displaced isopycnal surfaces or zonal velocity) reached at least down to about 250 m and covered the vertical extent of the low-DO cores. The estimated radii are 36 and 31 km and thus considerably smaller than the first baroclinic Rossby radius of around 90 km at these latitudes. For none of the 10 anticyclonic HBVs, we could identify any anticyclonic signature from satellite altimetry observations (Fig. 6a). One reason might be that the resolution of gridded SLA from conventional altimetry is not sufficient to resolve such small scale features. Another reason could be the fact that the eddies are strongly confined to the thermocline (below 30 – 50 m) and often do not have a surface signature.

4.4 Vertical structure of low-oxygen high-baroclinic mode vortices

The decomposition of a disturbed density profile into vertical baroclinic modes gives evidence about both the theoretical radius (Rossby radius) and propagation speed for this disturbed state (see section 3.1). Here, we did a vertical baroclinic mode analysis for the meridional section along 23°W between 6 and 12°N , which allowed us a direct comparison against the spatially resolved low-DO HBVs observed during the respective ship sections. The vertical structure of the first 20 baroclinic modes was obtained from the climatological hydrographic distribution (Fig. 7a to 7d). For all individual CTD-O profiles, we derived displacement profiles, ξ , and calculated vertical mode amplitudes x_n via modal decomposition (as described in section 3.1). We then clustered all x_n (i) related to a low-DO event (Table 1) and (ii) not related to a low-DO event (i.e. all other profiles along 23°W between 6 and 12°N), and calculated an average amplitude distribution (Figure 7e). For low-DO events, we found substantially enhanced amplitudes at all modes, but particularly at mode 2, 4, 7, 9 and 10 compared to the average amplitude distribution that is related to no low-DO events (Fig. 7e). These higher baroclinic modes $n = 4$ to 10 (exemplarily shown for 9°N , 23°W in Fig. 7a and 7c) for vertical displacement and pressure/horizontal velocity, respectively) have zero crossings in the upper few hundred meters, that are of similar vertical length scale compared to the vertical extent of



low-DO SCVs (near-surface to 250 m, see *section 4.2.1*). The lower baroclinic modes (e.g. mode 2) have a much larger vertical length scale and are not capable of describing the vertical structure that is related to low-DO HBVs. The corresponding Rossby radius of deformation for vertical baroclinic modes 4 to 10 was found from $R_{d,4} = 47$ km to $R_{d,10} = 18$ km at 6°N , 23°W and from $R_{d,4} = 24$ km to $R_{d,10} = 9$ km at 12°N , 23°W (Fig. 7g). These radii are well below the first baroclinic Rossby radius of deformation ($R_{d,1} = 152$ km at 6°N , 23°W and $R_{d,1} = 80$ km at 12°N , 23°W) and are close to the average radius of 34 km that was identified for the observed low-DO eddies (cf. Table 1 and *section 4.3*).

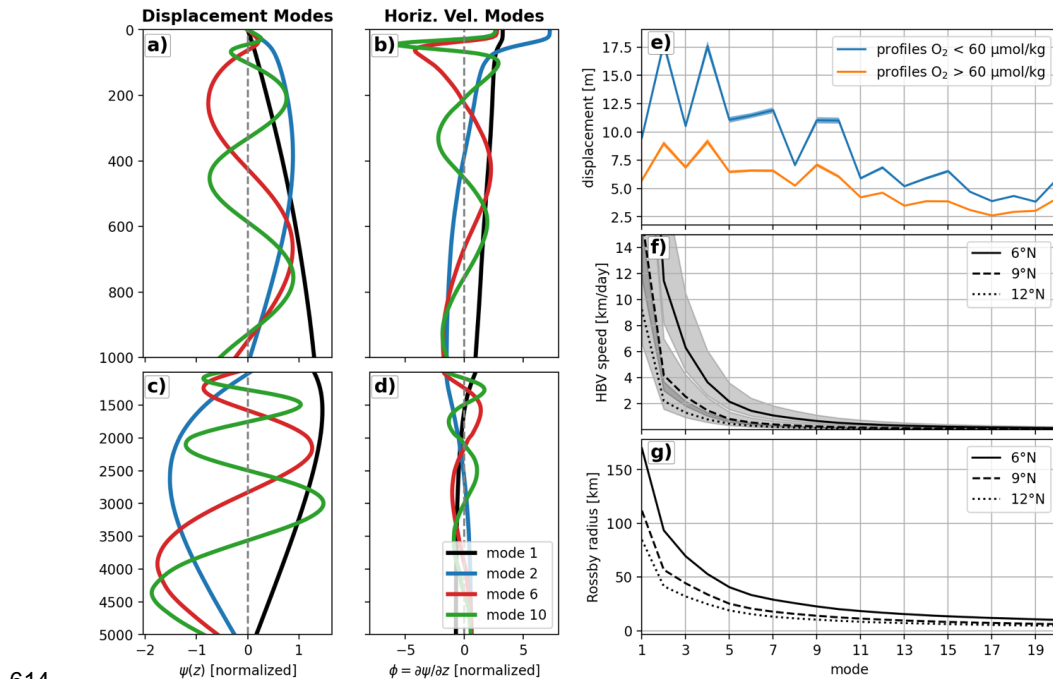


Figure 7: Dimensionless vertical structure functions of baroclinic modes 1, 2, 6 and 10 for (a, b) isopycnal displacement, Ψ_n , and (c, d) horizontal velocity, ϕ_n , obtained from the hydrographic profile of the World Ocean Atlas at 9°N , 23°W . (a) and (c) ((b) and (d)) show depth range 0 to 1000 m (1000 m to bottom). (e) Mean amplitudes of first 20 vertical displacement modes calculated through modal projection of hydrographic profiles from 23°W ship sections. Blue solid line denotes mean amplitude distribution, that is related to all hydrographic profiles with a minimum DO smaller than $60 \mu\text{mol kg}^{-1}$ in the upper 200 m (i.e. low-DO events that are summarized in Table 1). Orange solid line denotes mean amplitude distribution for all other hydrographic profiles along 23°W . Respective shadings denote standard error of the mean amplitude over all 1000 realizations. (f) Theoretical translation speed of high-baroclinic Rossby waves (HBVs) for the first 20 vertical modes between 6°N and 12°N along 23°W (see *equation 10*). The solid black line represents $Ro = 0.5$, while the shaded



area indicates the range $0.3 < Ro < 0.7$.
(g) Rossby radii of deformation for the first 20 vertical modes. In both (f) and (g), solid, dashed, and dotted lines correspond to values at 6°N , 9°N , and 12°N along 23°W , respectively.

4.5 Source waters of high-baroclonic mode vortices

The determination of the physical origin of subsurface HBVs, that are associated with the observed low-DO events, is not straight forward. A backtracking algorithm based on satellite altimetry observations as used in other studies for more poleward eddies (Chelton et al., 2011; Schütte et al., 2016a) is not applicable here, since these near-equatorial HBVs are hardly captured in the respective SLA products (Fig. 6). Instead, we derived water mass characteristics from all CTD-O profiles (Fig. 4a) located in the two boxes $[24^{\circ}\text{-}21^{\circ}\text{W}, 6^{\circ}\text{-}12^{\circ}\text{N}]$ and $[21^{\circ}\text{-}18^{\circ}\text{W}, 6^{\circ}\text{-}12^{\circ}\text{N}]$ for a conservative temperature range that corresponded to the depth range of the shallow DO minimum. A mean profile of absolute salinity was calculated for the two boxes and was used as a reference in order to calculate anomalies of absolute salinity as a function of potential density for every single CTD-O profile (Fig. 8). For both boxes, we clustered the salinity anomaly profiles into two classes, that were defined by the minimum DO concentration in the upper 200 m to be either below or above the threshold of $60 \mu\text{mol kg}^{-1}$.

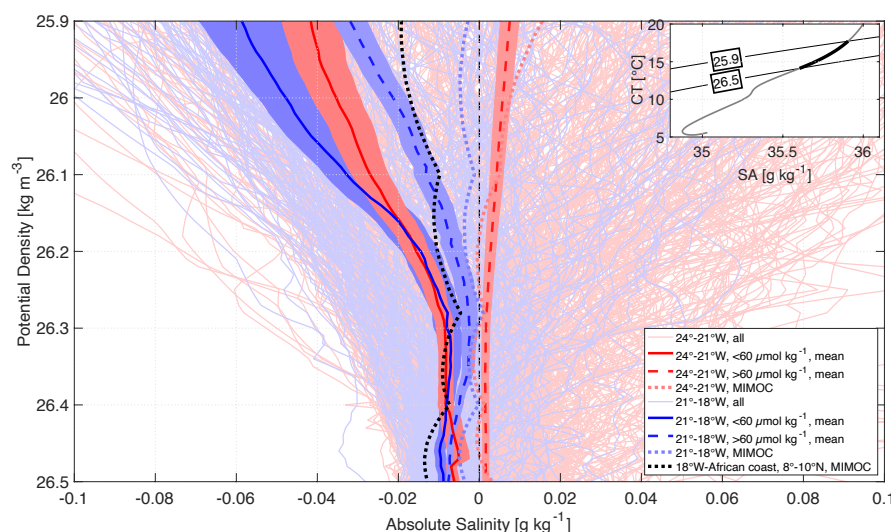


Figure 8: (Large panel) Anomalies of absolute salinity as a function of potential density in the eastern tropical North Atlantic for two different box regimes (Red: $24^{\circ}\text{-}21^{\circ}\text{W}$, $6^{\circ}\text{-}12^{\circ}\text{N}$ / Blue: $21^{\circ}\text{-}18^{\circ}\text{W}$, $6^{\circ}\text{-}12^{\circ}\text{N}$). The boxes are highlighted in Fig. 4. The anomalies are referenced to the mean profile of absolute salinity that was calculated from all hydrographic profiles found in both boxes. Thin solid lines denote all individual profiles and thick solid (dashed) lines show the average of the profiles, that are related to minimum DO concentrations below (above) $60 \mu\text{mol kg}^{-1}$ in the upper 200m. Shadings to the average profiles illustrate the respective



standard errors (see text for details). Blue and red dotted lines denote climatological profiles for the two boxes. Black dotted line shows the climatological profile for a third box (18°W-African coast, 8°-10°N), which defines the near-coastal regime off West-Africa. (Inlet panel) Mean characteristics of absolute salinity versus conservative temperature for the box 24°-18°W, 6°-12°N, taken from all CTD-O observations in this regime. Thick black line denotes the characteristics in the potential density range 25.9 to 26.5 kg m⁻³ and is the reference profile for the anomalies shown in the large panel.

Along-isopycnal gradients of mean salinity are weak (i.e. small spiciness) in the considered region [24°W-African coast, 6°-12°N], as shown by the water mass characteristics obtained from the climatological distribution (MIMOC) for the two boxes as well as for the near-coastal area east of them. The westward salinity increase along isopycnal surfaces is roughly 0.01 to 0.02 g kg⁻¹ per 5° (from the African coast at 17°W to about 22°W) in the potential density range between 26.1 and 26.4 kg m⁻³. This weak isopycnal gradient does not allow for a differentiation of water mass characteristics from individual CTD-O profiles.

However, water mass characteristics for low-DO and high-DO profiles were found to be significantly different from each other, when isopycnally averaging over all respective profiles. For the western box [24°-21°W, 6°-12°N], low-DO profiles were on average lower in salinity (compared to high-DO profiles) and they were found to be close to the average salinity anomaly profile from the eastern box [21°-18°W, 6°-12°N], suggesting that water masses related to low-DO profiles have their origin closer to the eastern boundary. However, the tropical low-DO extremes appear in the open ocean far away from the eastern boundary. The westward intensification of these events (*section 4.1*, Fig. 4), that are often related to HBVs (*section 4.2*), suggests an unexpected long isolation of the DO depleted water masses in the otherwise oxygen rich open ocean.

4.6 Origin & temporal evolution of high-baroclinic mode vortices based on model simulations

Outputs from the GFDL CM2.6 ocean model is used to investigate the origin and temporal evolution of these unusual vortices. We used the last 20 years of simulations for a regime similar to that considered in the shipboard observations. From Fig. 2, we already know that the model captures the main features of the mean state of the oxygen distribution. To assess whether low-oxygen events occur with similar frequency in the model and whether they are likewise associated with HBVs, we conducted analyses analogous to those performed on the observations (*Section 4.1*, Fig. 4; and *Section 4.3*, Fig. 6) using the model data.

First the horizontal DO distribution was calculated by taking the temporal and vertical (0-200 m) minimum of the simulated DO similar to the observations (Fig. 4b). In the latitude range 6°-12°N, lowest DO below 30 µmol kg⁻¹ is found close to the African coast (east of 18°W). In



687 general, the basin wide gradient of minimum DO is positive towards west, being in agreement
688 with the zonal gradient of the mean simulated DO distribution (Fig. 2b). Strikingly, minimum
689 DO is lower in the region 30°-24°W, 8°-12°N than in the region east of it (24°-21°W). The
690 threshold for the DO 10-percentile ($100 \mu\text{mol kg}^{-1}$) does not change over this longitude range,
691 whereas the mean DO distribution is increasing towards west (lower whiskers versus box
692 centers in Fig. 4d). The open ocean minimum of the DO distribution that is found in the region
693 30°-24°W, 8°-12°N is in good qualitative agreement (though located further west) with the
694 observed DO distribution (Fig. 4b versus Fig. 4a). In the longitude range 24°-21°W, low-oxygen
695 events are less likely.

696 From the GFDL CM2.6 model, we identified a HBV with a low-DO core in the near-equatorial
697 open ocean as exemplarily shown at the position 28°W, 10°N (Fig. 6h to 6n). The spatial extent
698 is comparable to our observational results (Fig. 6a to 6g). A meridional cross section through
699 the simulated HBV reveals the low-DO core at 80 m depth (isopycnal surface 26.5 kg m^{-3}) with
700 a lateral extent of about 1° in latitude and a vertical extent between about 50 and 150 m (Fig.
701 6i). The minimum DO is lower than $60 \mu\text{mol kg}^{-1}$, whereas DO outside the HBV is at values
702 above $150 \mu\text{mol kg}^{-1}$. Distributions of conservative temperature and potential density show
703 shallowing and deepening isopycnal surfaces above and below the DO minimum, respectively,
704 indicating a weakened stratification and consequently low PV at the low-DO core (Fig. 6j). The
705 HBV's velocity signature is strongly confined to subsurface depths and vanishes above 50 m
706 (Fig. 6k). In particular, surface velocity does not show any coherence with the subsurface
707 velocity field at depth of the HBV (Fig. 6h). This substantiates our observational results that
708 these HBVs can hardly be identified from the surface geostrophic velocity field obtained from
709 satellite observations. The HBV core exhibits low PV water, where minimum PV is found
710 slightly deeper than the DO minimum (Fig. 6l). This low PV water core is laterally isolated from
711 the surrounding high PV water, but also separated from the deeper low PV water through an
712 intermediate PV maximum along the isopycnal surface 26.7 kg m^{-3} . This isolation is the
713 prerequisite for a persistent eddy with a long-life time.

714 In the following, we present the temporal evolution of the HBV from the time of formation to the
715 decay. Fig. 9 shows model snapshots with horizontal maps of PV, relative vorticity normalized
716 by f (so that its magnitude is equal to Rossby number), DO and salinity for four different time
717 points throughout the HBV's lifetime. Fig. 10 shows time series of different physical and
718 biogeochemical variables for the HBV core position.

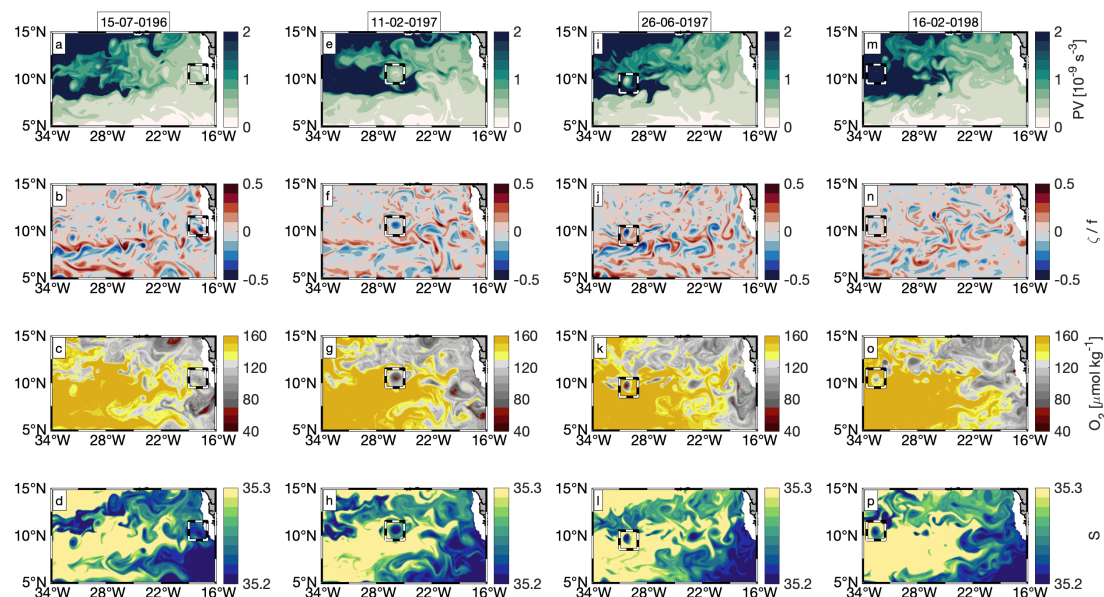
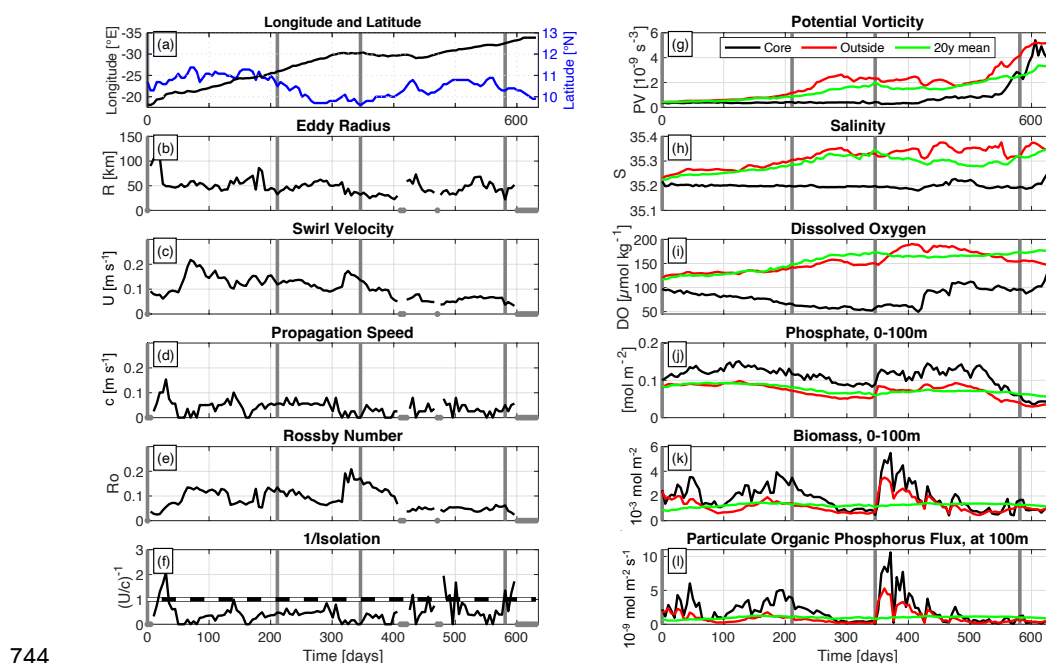


Figure 9: Model snapshots of PV on isopycnal surface 26.6 kg m^{-3} (top row), relative vorticity over f , DO and salinity on isopycnal surface 26.5 kg m^{-3} (second, third and fourth row) for different phases (different columns) of an anticyclonic HBV (respective time indicated above each column with $T = 0 / 211 / 346 / 580$ days: formation / strongest peculiarity / weakening / decay. Black-white dashed box in each sub panel denotes HBV position.

The HBV has its origin at the eastern boundary at 18°W , 10°N , where low PV water (Fig. 9a) with anticyclonic vorticity (Fig. 9b) is deflected offshore and provides the precondition for the eddy formation. The offshore deflected water carries typical water mass characteristics from the eastern boundary: low DO and low salinity (Fig. 9c and 9d). During westward propagation into the open ocean, the HBV enters high PV waters. 211 days after formation, it reaches 26°W , 10.5°N with low PV (Fig. 9e) and high negative relative vorticity (Fig. 9f) in its core. The coherent eddy is strongly isolated from surrounding high PV water as shown by the intensified DO minimum (Fig. 9g) and low salinity (Fig. 9h) in its core. In the following 5 months the HBV propagates further westward, but is disturbed by high PV water, that is advected from the western tropical Atlantic. This leads to a weakening of the HBV with a smaller low PV core (Fig. 9i), but still carrying pronounced negative relative vorticity (Fig. 9j), low DO (Fig. 9k) and low salinity (Fig. 9l) compared to surrounding water. The HBV eventually loses its energy and decays about 580 days after formation at 33°W , 10°N (Fig. 9m and 9n), where the core water still appears with anomalous low DO and salinity (Fig. 9o and 9p).



739 The quick offshore deflection of coastal water, that is associated with the HBV's formation, is
740 illustrated by the strong change in longitude (Fig. 10a) and by the high propagation speed (Fig.
741 10d) during the first 50 days. This deflection is more like a pulse rather than an offshore
742 transport of enclosed water ($(U/c)^{-1} > 1$, Fig. 10f), where the HBV stabilizes after that time at
743 a radius of 50 km (Fig. 10b).



744

745 Figure 10: Time series of different variables related to the core of the modelled subsurface
746 intensified eddy shown in Figs. 4h-4n and Fig. 8. Time is given as elapsed days since eddy
747 detachment from the African coast. Vertical gray lines in each panel denote time points for
748 horizontal maps shown in Fig. 8 (0, 211, 346 and 581 days). (a) longitude (black line) and
749 latitude (blue line), (b) Eddy radius, (c) Eddy swirl velocity, (d) Eddy propagation speed, (e)
750 Rossby number, (f) Inverse of isolation parameter (black line). Black-white dashed line denotes
751 threshold, below which the water is trapped in the eddy core (swirl velocity > propagation
752 speed). (g) Potential vorticity, (h) salinity, (i) DO, (j) phosphate, (k) biomass, (l) flux of
753 particulate organic phosphorus. Variables are given for the following layers. In panels (a)-(f)
754 and (h)-(i): isopycnal surface 26.5 kg m⁻³. In panel (g): isopycnal surface 26.6 kg m⁻³. In panels
755 (j)-(k): integral over 0-100 m. (l) at 100 m. For the right column (panels (g)-(l)), black lines show
756 value in eddy core, red lines show mean values outside the eddy (average between 1° and 3°
757 of longitude/latitude around the eddy core position) and green lines show 20-year model mean
758 that is given at the respective position of the eddy core. In panels (b)-(f), gray dots at zero line
759 denote time points, where no estimate was possible.

760 From day 80 to day 300, the HBV continuously propagates westward until 30°W with only slight
761 changes in latitude (10°-11°N), at a propagation speed of 0.7 m s⁻¹, a swirl velocity between
762 0.1 and 0.2 m s⁻¹ and a radius of 50 km (Rossby number between 0.1 and 0.2) (Fig. 10a-10f).
763 The strong isolation ($(U/c)^{-1} < 1$) over that time keeps the core water constantly low in PV



764 and salinity, while surrounding waters increase in PV and salinity during eddy westward
765 propagation (Fig. 10g-10h). DO continuously decreases from $97 \mu\text{mol kg}^{-1}$ to $54 \mu\text{mol kg}^{-1}$ over
766 300 days which yields an average DO consumption of $0.14 \mu\text{mol kg}^{-1} \text{d}^{-1}$ (Fig. 10i). In the upper
767 part of the eddy, enhanced nutrient concentration is associated with increased biomass
768 production, which leads to enhanced export of organic matter between days 100 and 300 (Fig.
769 10j-10l). The associated increased respiration and the strong isolation both lead to the
770 development of this substantial DO deficient zone. The high PV water, that is advected from
771 the west, acts as a barrier for the HBV and westward propagation stops after day 300 (Fig.
772 10a and 10d). The HBV is deformed by the high PV water, which likely leads to enhanced
773 isopycnal and diapycnal mixing at the eddy periphery. In fact, the HBV shrinks between days
774 300 and 400 as illustrated by the continuously decreasing radius from 50 km to 30 km (Fig.
775 10b). Though, the core still shows source water characteristics with unaltered low PV and low
776 salinity, and still holds the DO deficient zone. After day 400, the SCV starts to interact with
777 surrounding water - partly being low in PV as well - which weakens the isolation of the HBV
778 core ($(U/c)^{-1} \approx 1$, Fig. 10f) and leads to continuous increase of PV and DO. PV strongly
779 increases after day 550 and reaches the PV threshold of surrounding water at about day 600,
780 where the core starts to dissolve as illustrated by the strong increase of salinity and DO after
781 day 600.

782 5 Discussion

783 Moored time series of dissolved oxygen (DO) in the near-equatorial Atlantic (4°N up to 12°N)
784 occasionally show pronounced dips in oxygen concentrations falling significantly beneath the
785 climatological mean, well below the mixed layer and lasting for several weeks. In addition, we
786 found that about 8% of all observed CTD-O profiles in the near-equatorial ETNA (25° - 15°W ,
787 6° - 12°N) appear with anomalous low-DO ($< 60 \mu\text{mol kg}^{-1}$) in the upper 200 m, which is as well
788 below the climatological DO concentration. Until now, the causes of these extreme low-DO
789 events have remained unclear. Mesoscale eddies with low oxygen cores - known to occur
790 farther north around 20°N - are not expected to drive such extensive oxygen-deficient zones
791 in the near-equatorial region, as they are not believed to persist here as coherent vortices with
792 lifespans of several months or longer (Chaigneau et al., 2009; Keppler et al., 2018). However,
793 the majority of these low-DO events (60%) are clearly associated with high-baroclinic
794 subsurface-intensified eddies (Table 1, Fig. 4, Fig. 5). For the remaining 40%, the velocity and
795 density distributions did not reveal clear eddy signatures, nor did satellite data - consistent with
796 all identified vortices, which generally lack a distinct surface signature. However, a connection
797 to subsurface-intensified eddies cannot be ruled out a priori for these cases.

798 This underlines that in understanding the Earth system, a better understanding of small-scale



799 ocean dynamics (smaller than the first baroclinic Rossby radius of deformation) is essential,
800 as they play a crucial role in the distribution of energy and tracers as well as the regulation of
801 biogeochemical processes. In particular, below the surface layer - where satellite observations
802 are ineffective - our understanding of the frequency, magnitude, and impact of these small-
803 scale ocean dynamics remains limited.

804 In the vicinity of the equator ($< 5^{\circ}\text{N/S}$), mesoscale dynamics dominantly appear as horizontally
805 anisotropic waves (e.g. tropical instability waves) rather than closed circular structures. These
806 wave-like structures, however, are not isolated enough to effectively transport or develop low-
807 oxygen environments. The eddies with DO anomalies that we observed are relatively small
808 and long-lived high-baroclinic vortices (HBVs). Ship sections along 23°W exclusively revealed
809 anticyclonic HBVs, whereas both anticyclonic and cyclonic HBVs were found from moored
810 observations at 11°N , 21°W and in the model.

811 **5.1 Vertical and horizontal structure of the low-oxygen events and the associated** 812 **high-baroclinic mode vortices**

813 The observed anticyclonic HBVs had a pronounced low-DO core that vertically extended from
814 the base of the mixed layer down to several hundred meter depth (with minimum DO at depths
815 between 45 and 90 m). The anomalous horizontal velocity of the observed anticyclonic HBVs
816 was at maximum (maximum EKE) at the depth of the DO minimum and extended from 50 to
817 roughly 250 m. Stratification in the observed anticyclonic HBVs' core was weak over this depth
818 range with upward and downward displaced isopycnals above and below the depth of EKE
819 maximum, respectively. We found an average radius of about 34 km (between 20 and 45 km)
820 for the observed HBVs. A decomposition into vertical baroclinic modes showed, that modes 4
821 to 10 fit best to low-DO events that are related to these HBVs. The associated 4th to 10th
822 baroclinic Rossby radii of deformation are between 34 and 13 km (at 9°N) and in good
823 agreement with the observed eddy radii. The observed radii appear well below the first
824 baroclinic Rossby radius of deformation (more than 100 km in the region) and corresponding
825 eddies can be considered as higher baroclinic mode vortices. Rossby numbers were below 1
826 (about 0.3 – 0.7 found from shipboard observations; 0.4 found in the GFDL CM2.6 model
827 simulation).

828 The observed cyclonic HBVs appeared with a stratification maximum at about 150 m and a
829 cyclonic velocity structure with maximum EKE at a similar depth. Shallow DO minima were
830 found at 100 and 200 m throughout the transition, but without any clear separation from the
831 deep OMZ at 300 m. This less intensified DO minimum at 100 m and the missing intermediate
832 DO maximum at 200 m is a substantial difference to the DO distribution observed within



833 anticyclonic HBVs. However, enhanced DO consumption has been shown to be a reasonable
834 driver for DO depletion in a cyclonic HBV, that was observed in the western subtropical North
835 Atlantic (Li et al., 2008). Pure upwelling or upward mixing of low-DO water from the deep OMZ
836 cannot explain such vertically homogeneous distribution of low-DO between 100 and 300 m in
837 cyclonic HBVs. These processes would imply either a shallowing of isopycnal surfaces or a
838 weakened stratification within this depth range, which is contradictory to the observed
839 deepening of isopycnals above 150 m, shallowing of isopycnals below 150 m and
840 consequently the intensified stratification at 150 m (Fig. 5, Event #03). Due to the increased
841 stratification, the thickness of the intermediate DO maximum layer (that is associated with
842 isopycnal 26.6 kg m^{-3}) is reduced and very likely not resolved by the sparsely distributed
843 number of DO sensors.

844 We could not collocate any clear signals in SLA or SST from satellite observations with the in
845 situ observed HBVs. Shipboard observations showed a strongly weakening velocity signature
846 toward the surface. Also the simulated HBVs from GFDL CM2.6 model showed similar
847 characteristics as the observed vortices and no signature could be found from the surface
848 velocity. Moreover, the resolution and interpolation scheme for the gridded SLA data likely do
849 not allow to properly capture geostrophic structures at scales of smaller than about 40 km.
850 These are likely reasons, why near-equatorial subsurface eddies are hardly identified from
851 satellite products. If higher resolution satellite products from SWOT will allow to detect the
852 HBVs remains to be seen, though what we see from the in-situ observed structure and the
853 model results we conjecture that the high baroclinic mode HBVs tend to “hide” below the
854 surface/mixed layer base.

855 **5.2 Origin, lifetime & evolution of the oxygen content of high-baroclinic mode** 856 **vortices**

857 Water mass characteristics derived from shipboard observations showed that open ocean
858 water masses with DO below $60 \mu\text{mol kg}^{-1}$ in the upper 200 m (often associated with HBVs)
859 likely originate from the eastern boundary, where SACW contributions exceed those of NACW.
860 Model results are in agreement as they show the formation of a low-DO HBVs with low PV in
861 its core off the African coast at about 10°N , 18°W . Hence, it is expected that the generation
862 mechanism is consistent with previous studies on HBV formation, in which the interaction
863 between the mean flow and sharp topographic curvature leads to the formation low-PV waters
864 within the bottom boundary layer, and the shedding of HBVs (D’Asaro, 1988; Molemaker et
865 al., 2015; Thomsen et al., 2016; Srinivasen et al., 2017; Dilmahamod et al., 2022).

866 The simulated HBV analyzed here propagated westward far into the open ocean over a



867 distance of 1,600 km (10°N, 33°W) and lasted for 600 days (average propagation speed of
868 2.6 km day⁻¹). For the observed HBVs, we could not derive propagation speeds in a similar
869 way. Instead, we followed an approach by Nof (1981) and Rubino et al. (2009), who formulated
870 the westward translation of isolated high baroclinic eddies on a plane, which is given as a
871 function of the n -th baroclinic Rossby radius of deformation and the Rossby number:

$$C_n = -\frac{1}{3}\beta R_{d,n}^2(1 - Ro)^{-1} \quad (2)$$

872 with β being the meridional derivative of the Coriolis parameter. Considering a Rossby radius
873 between 35 and 50 km and a Rossby number between 0.3 and 0.7 (taken as characteristic
874 scales from the observed HBVs corresponding to the vertical baroclinic mode 4) yields a
875 propagation speed between 1.1 and 5.4 km day⁻¹. This is in good agreement with the
876 propagation speed obtained from the simulated HBV. Considering the origin of the observed
877 low-DO HBVs at the eastern boundary (cf. *section 4.4*), a propagation speed at 1.1-5.4
878 km day⁻¹ yields a propagation time of 100 to 500 days to propagate a distance toward 23°W
879 (around 550 km). The fact, that these high baroclinic low-DO HBVs are not captured by satellite
880 products, prevents both backtracking to their origin and estimating their lifetime directly.
881 However, assuming that the HBVs origin close to the African coast and propagate westward
882 at 1.8 to 4.9 km day⁻¹, they would require approximately 110 to 300 days to travel the 550 km
883 distance to 23°W.

884 In contrast to anticyclonic HBVs, cyclonic HBVs only twice in the mooring time series and were
885 not found in any of the numerous ship sections along 23°W. We may only speculate, that
886 cyclonic HBVs do not frequently propagate across 23°W due to a much more reduced eddy
887 life time. They transport anomalously high PV water in their core compared to surrounding
888 water masses. During westward propagation, the isolation of the core is expected to be
889 reduced due to the westward increasing PV background gradient in the tropical Atlantic. As
890 anticyclonic HBVs propagate westward, their low-PV cores are reinforced and remain isolated
891 from surrounding waters, promoting their longevity. However, encounters with high-PV water
892 from the western basin may destabilize them, while interactions with other low-PV anticyclones
893 can enhance their stability. Throughout the long lifetime of the simulated anticyclonic HBVs,
894 enhanced respiration in the eddy core leads to a strong DO decrease from 92 to 46 $\mu\text{mol kg}^{-1}$
895 over a period of 260 days, yielding a DO consumption of 0.18 $\mu\text{mol kg}^{-1} \text{ d}^{-1}$. This fits to our
896 observational results, where lowest absolute DO concentrations occurred in the open ocean
897 (24°-21°W) rather than in the region that is located closer to the eastern boundary (21°-18°W).
898 The here found DO consumption rates are also in good agreement with consumption rates
899 estimated from observed subsurface intensified anticyclonic eddies ($0.19 \pm 0.08 \mu\text{mol kg}^{-1} \text{ d}^{-1}$)



that originate from the Mauritanian upwelling system and propagate westward at about 18°N (Schütte et al., 2016). We shall note, that DO was observed close to anoxic conditions on the shelf of Senegal at about 14°N at depths of about 20 m (Machu, 2019). However, these water masses are at much shallower depth and lighter densities and are very likely not the source region for the low-DO core of the here described offshore HBVs. However, the here described low-DO eddies, characterized with low PV waters in their cores, likely have their origin at the eastern boundary with the bottom boundary layer identified as the source of this low PV waters.

6 Summary and conclusion

We shall summarize the following take home messages to the reader:

(i) Distribution and occurrence of low-DO events:

In the near-equatorial North Atlantic (25°-15°W, 6°-12°N), about 8% of all CTD-O profiles occur with a DO concentration of less than 60 $\mu\text{mol kg}^{-1}$ in the upper 200 m, which is well below the climatological DO concentration. These extreme low-DO events are more frequent and more intensified in the open ocean (30°-21°W) compared to the region east of it (21°- coast of West Africa). Unprecedented low-DO concentrations were found with 1 $\mu\text{mol kg}^{-1}$ at 80 m depth at the mooring located at 11°N 23W as well as 17 $\mu\text{mol kg}^{-1}$ (8°N, 23°W) and 29 $\mu\text{mol kg}^{-1}$ (9°N, 21°W) observed with ship based measurements.

(ii) Low-DO events are related to subsurface intensified submesoscale coherent vortices:

We found 66% of open ocean low-DO events to be related to subsurface intensified submesoscale coherent vortices, where anticyclonic rotation appeared as the dominant eddy type. These vortices have a high baroclinic vertical structure, associated to vertical baroclinic modes 4 to 10, and are confined to the upper 250 m. In situ velocity observations revealed an average radius of 34 km, which is well below the first baroclinic Rossby radius of deformation ($O(100 \text{ km})$), but agrees well with Rossby radii of the higher baroclinic modes 4 to 10 (34 to 13 km at 9°N). Despite the small length scales, the Rossby number of the vortices is below 1, assigning them to the dynamical range of mesoscale variability.

(iii) Origin and life time:

The vortices most likely originate from the eastern boundary. They can propagate far into the open ocean with a propagation speed of 1.8 - 4.9 km day^{-1} , reaching a life time of more than half a year (it took around 100 to 500 days to propagate the 550km distance towards 23°W). This is much longer than currently suggested considering the highly dynamical area and the proximity to the equator. Model simulations even show a life time of up to 1.5 years. Cyclonic eddies with low-



935 oxygen cores were less frequent than anticyclonic eddies. Cyclonic eddies were
936 not found in ship sections along 23°W, but in the minority of all low-DO extreme
937 events from moored observations at 11°N, 21°W.

938 (iv) Impact of the vortices on DO and biogeochemistry:

939 The unexpected long-life times of the near-equatorial vortices goes along with a
940 strong isolation of their low-PV core from surrounding water. These vortices are
941 capable of forming a DO deficient zone in their core, since enhanced primary
942 production and remineralisation leads to increased DO consumption ($0.18 \mu\text{mol kg}^{-1}$
943 day^{-1} at least for the simulated anticyclonic vortices).

944 (v) Detection of near-equatorial vortices with remote sensing satellites:

945 Near-equatorial vortices are hardly detectable by conventional satellite altimetry
946 observations, which precludes a backtracking of these eddies. New observations
947 are desirable to verify whether the new SWOT mission can capture such SCV,
948 although a strong surface signal is not expected due to the mainly subsurface
949 structure (also supported by the model).

950 Subsurface coherent vortices in the near-equatorial ocean have been so far overlooked in
951 driving DO deficient zones. The long-lived vortices appear unexpectedly quite regularly given
952 theoretical considerations and are able to generate hypoxic regimes in the open ocean, which
953 may impact on pelagic fish, biodiversity and biogeochemical cycles. They are typically not
954 traceable in satellite products, which makes a collocation of satellite data with in-situ
955 observations (CTD-O, Argo profiles, moored observations) hardly possible. The comparatively
956 coarse resolution of satellite observations might instead lead to a wrong collocation of the
957 subsurface low-DO events with larger surface intensified mesoscale structures nearby. The
958 mechanisms for the generation of these near-equatorial low-DO eddies remain an open
959 question. So far, we here identified a potential source region and provided a first insight about
960 the dynamics (life time, baroclinicity, isolation) of these eddies. A more comprehensive
961 investigation from high resolution ocean circulation models - coupled to biogeochemistry -
962 would shed light onto the generation. Further, the study of the temporal evolution of dominant
963 vertical baroclinic modes throughout the eddies' life cycle would contribute to a better
964 understanding of the eddy dynamics and stability. Moreover, the interdisciplinary view on
965 changes in biogeochemical processes would increase the understanding about the impact on
966 biogeochemistry. The in-situ tracking and observation of these eddies over their life cycle is
967 challenging, but would provide key information to validate the simulation of these eddies.

968

969



970 **7 Data availability**

971 The assembled shipboard measurements (27 research cruises) and moored data used in this
972 paper are available and collected at <https://doi.pangaea.de/XXXX>. The used satellite altimetry
973 data is provided by Marine Copernicus (<https://marine.copernicus.eu>) can be downloaded at
974 <https://doi.org/10.48670/moi-00148>. The used gridded climatological hydrography and oxygen
975 from the World Ocean Atlas 2023 (WOA23), is available at NOAA under:
976 <https://doi.org/10.25921/va26-hv25>. The monthly, isopycnal and mixed-layer ocean
977 climatology (MIMOC) used is available at <https://www.pmel.noaa.gov/mimoc/>. The Model data
978 will be made openly accessible via the GEOMAR website <https://data.geomar.de> where data
979 is uniquely identifiable via handle assignment (PID) and will be accessible per download.

980 **Author contributions**

981 Conceptualization: FS, JH, PB, Data curation: JH, IF, FS, Formal analysis and methodology:
982 JH, IF, MS, FS, AB, FD, Funding acquisition: PB, Writing – original draft: JH, FS, IF, Writing
983 – review and editing: FS, JH, IF, AB, FD, MS, PB

984

985 **Competing interests**

986 The contact author has declared that none of the authors has any competing interests.

987

988 **Acknowledgements**

989 We thank the crew and the “Leitstelle Deutsche Forschungsschiffe” for supporting the numerous
990 expeditions in the eastern tropical North Atlantic that have made this work possible. Research cruises
991 with RV Meteor, RV Maria S. Merian were funded by the Deutsche Forschungsgemeinschaft as part of
992 Sonderforschungsbereich 754 “Climate-Biogeochemistry Interactions in the Tropical Ocean” and
993 through other projects such as the EU H2020 TRIATLAS project (grant agreement 817578) funded by
994 the German Federal Ministry of Education and Research (BMBF). Moored velocity and oxygen
995 observations were partly acquired in cooperation with the PIRATA project, and we would like to thank
996 B. Bourlès, R. Lumpkin, C. Schmid, and G. Foltz for their help with mooring work and data sharing. We
997 thank the captains and crew of the RV *Maria S. Merian*, RV *Meteor*, RV *Poseidon*, and RV *L’Atalante* as
998 well as our technical group for their help with the fieldwork.



References

- Antonov, J. I., Seidov, D., Boyer, T. P., Locarnini, R. A., Mishonov, A. V., Garcia, H. E., Baranova, O. K., Zweng, M. M., and Johnson, D. R.: *World Ocean Atlas 2009, Volume 2: Salinity*. S. Levitus, Ed. NOAA Atlas NESDIS 69, U.S. Government Printing Office, Washington, D.C., 184 pp, 2010.
- Bittig, H. C., Körtzinger, A., Neill, C., van Ooijen, E., Plant, J. N., Hahn, J., Johnson, K. S., Yang, B., and Emerson, S. R.: Oxygen Optode Sensors: Principle, Characterization, Calibration, and Application in the Ocean, *Frontiers in Marine Science*, 4, 10.3389/fmars.2017.00429, 2018.
- Brandt, P., Hormann, V., Körtzinger, A., Visbeck, M., Krahmann, G., Stramma, L., Lumpkin, R., and Schmid, C.: Changes in the Ventilation of the Oxygen Minimum Zone of the Tropical North Atlantic, *J. Phys. Oceanogr.*, 40, 1784-1801, 10.1175/2010jpo4301.1, 2010.
- Brandt, P., Bange, H. W., Banyte, D., Dengler, M., Didwischus, S. H., Fischer, T., Greatbatch, R. J., Hahn, J., Kanzow, T., Karstensen, J., Körtzinger, A., Krahmann, G., Schmidtke, S., Stramma, L., Tanhua, T., and Visbeck, M.: On the role of circulation and mixing in the ventilation of oxygen minimum zones with a focus on the eastern tropical North Atlantic, *Biogeosciences*, 12, 489-512, 10.5194/bg-12-489-2015, 2015.
- Calil, P. H. R.: High-Resolution, Basin-Scale Simulations Reveal the Impact of Intermediate Zonal Jets on the Atlantic Oxygen Minimum Zones. *Journal of Advances in Modeling Earth Systems*, 15(2), e2022MS003158.
<https://agupubs.onlinelibrary.wiley.com/doi/abs/10.1029/2022MS003158>, 2023
- Chaigneau, A., Eldin, G., and Dewitte, B.: Eddy activity in the four major upwelling systems from satellite altimetry (1992-2007), *Prog. Oceanogr.*, 83, 117-123, 10.1016/j.pocean.2009.07.012, 2009.
- Chelton, D. B., deSzoeke, R. A., Schlax, M. G., Naggar, K. E., and Siwertz, N.: Geographical Variability of the First Baroclinic Rossby Radius of Deformation, *J. Phys. Oceanogr.*, 28, 433-460, 10.1175/1520-0485(1998)028<0433:Gvotfb>2.0.Co;2, 1998.
- Chelton, D. B., Schlax, M. G., and Samelson, R. M.: Global observations of nonlinear mesoscale eddies, *Prog. Oceanogr.*, 91, 167-216, 10.1016/j.pocean.2011.01.002, 2011.
- Christiansen, S., Hoving, H. J., Schutte, F., Hauss, H., Karstensen, J., Kortzinger, A., Schroder, S. M., Stemann, L., Christiansen, B., Picheral, M., Brandt, P., Robison, B., Koch, R., and Kiko, R.: Particulate matter flux interception in oceanic mesoscale eddies by the polychaete *Poeobius* sp, *Limnol. Oceanogr.*, 63, 2093-2109, 10.1002/lno.10926, 2018.
- D'Asaro, E. A.: Generation of submesoscale vortices: A new mechanism, *Journal of Geophysical Research: Oceans*, 93, 6685-6693, 10.1029/JC093iC06p06685, 1988.
- Delworth, T. L., Rosati, A., Anderson, W., Adcroft, A. J., Balaji, V., Benson, R., Dixon, K., Griffies, S. M., Lee, H.-C., Pacanowski, R. C., Vecchi, G. A., Wittenberg, A. T., Zeng, F., and Zhang, R.: Simulated Climate and Climate Change in the GFDL CM2.5 High-Resolution Coupled Climate Model, *J. Clim.*, 25, 2755-2781, 10.1175/jcli-d-11-00316.1, 2012.
- Dilmahamod, A. F., J. Karstensen, H. Dietze, U. Löptien, and K. Fennel, 2022: Generation Mechanisms of Mesoscale Eddies in the Mauritanian Upwelling Region. *J. Phys. Oceanogr.*, 52, 161–182, <https://doi.org/10.1175/JPO-D-21-0092.1>.



Dufour, C. O., Griffies, S. M., de Souza, G. F., Frenger, I., Morrison, A. K., Palter, J. B., Sarmiento, J. L., Galbraith, E. D., Dunne, J. P., Anderson, W. G., and Slater, R. D.: Role of Mesoscale Eddies in Cross-Frontal Transport of Heat and Biogeochemical Tracers in the Southern Ocean, *J. Phys. Oceanogr.*, 45, 3057-3081, 10.1175/jpo-d-14-0240.1, 2015.

Duteil, O., Schwarzkopf, F. U., Böning, C. W., and Oschlies, A.: Major role of the equatorial current system in setting oxygen levels in the eastern tropical Atlantic Ocean: A high-resolution model study, *Geophys. Res. Lett.*, 41, 2033-2040, 10.1002/2013gl058888, 2014.

Eden, C.: Eddy length scales in the North Atlantic Ocean, *J. Geophys. Res.-Oceans*, 112, 10.1029/2006jc003901, 2007.

Fiedler, B., Grundle, D. S., Schütte, F., Karstensen, J., Löscher, C. R., Hauss, H., Wagner, H., Loginova, A., Kiko, R., Silva, P., Tanhua, T., and Körtzinger, A.: Oxygen utilization and downward carbon flux in an oxygen-depleted eddy in the eastern tropical North Atlantic, *Biogeosciences*, 13, 5633-5647, 10.5194/bg-13-5633-2016, 2016.

Fischer, J., Brandt, P., Dengler, M., Müller, M., and Symonds, D.: Surveying the Upper Ocean with the Ocean Surveyor: A New Phased Array Doppler Current Profiler, *J. Atmos. Ocean. Technol.*, 20, 742-751, 10.1175/1520-0426(2003)20<742:Stuowt>2.0.Co;2, 2003.

Frenger, I., Bianchi, D., Stührenberg, C., Oschlies, A., Dunne, J., Deutsch, C., Galbraith, E., and Schütte, F.: Biogeochemical Role of Subsurface Coherent Eddies in the Ocean: Tracer Cannonballs, Hypoxic Storms, and Microbial Stewpots?, *Glob. Biogeochem. Cycle*, 32, 226-249, doi:10.1002/2017GB005743, 2018.

Galbraith, E. D., Dunne, J. P., Gnanadesikan, A., Slater, R. D., Sarmiento, J. L., Dufour, C. O., de Souza, G. F., Bianchi, D., Claret, M., Rodgers, K. B., and Marvasti, S. S.: Complex functionality with minimal computation: Promise and pitfalls of reduced-tracer ocean biogeochemistry models, *Journal of Advances in Modeling Earth Systems*, 7, 2012-2028, 10.1002/2015ms000463, 2015.

Garcia, H. E., Locarnini, R. A., Boyer, T. P., Antonov, J. I., Baranova, O. K., Zweng, M. M., and Johnson, D. R.: *World Ocean Atlas 2009, Volume 3: Dissolved Oxygen, Apparent Oxygen Utilization, and Oxygen Saturation*. S. Levitus, Ed. NOAA Atlas NESDIS 70, U.S. Government Printing Office, Washington, D.C., 344 pp, 2010a.

Garcia, H. E., Locarnini, R. A., Boyer, T. P., Antonov, J. I., Zweng, M. M., Baranova, O. K., and Johnson, D. R.: *World Ocean Atlas 2009, Volume 4: Nutrients (phosphate, nitrate, silicate)*. S. Levitus, Ed. NOAA Atlas NESDIS 71, U.S. Government Printing Office, Washington, D.C., 398 pp., 2010b.

Gill, A. E.: *Atmosphere-Ocean Dynamics*, International Geophysics Series Volume 30, Academic Press, New York, 1982.

Griffies, S. M., Winton, M., Anderson, W. G., Benson, R., Delworth, T. L., Dufour, C. O., Dunne, J. P., Goddard, P., Morrison, A. K., Rosati, A., Wittenberg, A. T., Yin, J., and Zhang, R.: Impacts on Ocean Heat from Transient Mesoscale Eddies in a Hierarchy of Climate Models, *J. Clim.*, 28, 952-977, 10.1175/jcli-d-14-00353.1, 2015.

Gula, J., Blacic, T. M., and Todd, R. E.: Submesoscale Coherent Vortices in the Gulf Stream, *Geophys. Res. Lett.*, 46, 2704-2714, 10.1029/2019gl081919, 2019.

Hahn, J., Brandt, P., Greatbatch, R. J., Krahmann, G., and Kortzinger, A.: Oxygen variance and meridional oxygen supply in the Tropical North East Atlantic oxygen minimum zone, *Clim. Dyn.*, 43, 2999-3024, 10.1007/s00382-014-2065-0, 2014.



Hahn, J., Brandt, P., Schmidtke, S., and Krahmann, G.: Decadal oxygen change in the eastern tropical North Atlantic, *Ocean Science*, 13, 551-576, 10.5194/os-13-551-2017, 2017.

Hauss, H., Christiansen, S., Schütte, F., Kiko, R., Lima, M. E., Rodrigues, E., Karstensen, J., Loscher, C. R., Kortzinger, A., and Fiedler, B.: Dead zone or oasis in the open ocean? Zooplankton distribution and migration in low-oxygen medowater eddies, *Biogeosciences*, 13, 1977-1989, 10.5194/bg-13-1977-2016, 2016.

Karstensen, J., Stramma, L., and Visbeck, M.: Oxygen minimum zones in the eastern tropical Atlantic and Pacific oceans, *Prog. Oceanogr.*, 77, 331-350, 10.1016/j.pocean.2007.05.009, 2008.

Karstensen, J., Fiedler, B., Schütte, F., Brandt, P., Kortzinger, A., Fischer, G., Zantopp, R., Hahn, J., Visbeck, M., and Wallace, D.: Open ocean dead zones in the tropical North Atlantic Ocean, *Biogeosciences*, 12, 2597-2605, 10.5194/bg-12-2597-2015, 2015.

Karstensen, J., Schütte, F., Pietri, A., Krahmann, G., Fiedler, B., Grundle, D., Hauss, H., Kortzinger, A., Löscher, C. R., Testor, P., Vieira, N., and Visbeck, M.: Upwelling and isolation in oxygen-depleted anticyclonic medowater eddies and implications for nitrate cycling, *Biogeosciences*, 14, 2167-2181, 10.5194/bg-14-2167-2017, 2017.

Keppler, L., Cravatte, S., Chaigneau, A., Pegliasco, C., Gourdeau, L., and Singh, A.: Observed Characteristics and Vertical Structure of Mesoscale Eddies in the Southwest Tropical Pacific, *Journal of Geophysical Research: Oceans*, 123, 2731-2756, 10.1002/2017jc013712, 2018.

Key, R. M., Kozyr, A., Sabine, C. L., Lee, K., Wanninkhof, R., Bullister, J. L., Feely, R. A., Millero, F. J., Mordy, C., and Peng, T.-H.: A global ocean carbon climatology: Results from Global Data Analysis Project (GLODAP), *Glob. Biogeochem. Cycle*, 18, 10.1029/2004gb002247, 2004.

Köhn, E. E., Greatbatch, R. J., Brandt, P., and Claus, M.: The formation and ventilation of an oxygen minimum zone in a simple model for latitudinally alternating zonal jets, *Ocean Sci.*, 20, 1281-1290, <https://doi.org/10.5194/os-20-1281-2024>, 2024.

Li, Q. P., Hansell, D. A., McGillicuddy Jr., D. J., Bates, N. R., and Johnson, R. J.: Tracer-based assessment of the origin and biogeochemical transformation of a cyclonic eddy in the Sargasso Sea, *Journal of Geophysical Research: Oceans*, 113, 10.1029/2008jc004840, 2008.

Locarnini, R. A., Mishonov, A. V., Antonov, J. I., Boyer, T. P., Garcia, H. E., Baranova, O. K., Zweng, M. M., and Johnson, D. R.: *World Ocean Atlas 2009, Volume 1: Temperature*. S. Levitus, Ed. NOAA Atlas NESDIS 68, U.S. Government Printing Office, Washington, D.C., 184 pp, 2010.

Löscher, C. R., Fischer, M. A., Neulinger, S. C., Fiedler, B., Philippi, M., Schütte, F., Singh, A., Hauss, H., Karstensen, J., Kortzinger, A., Künzel, S., and Schmitz, R. A.: Hidden biosphere in an oxygen-deficient Atlantic open-ocean eddy: future implications of ocean deoxygenation on primary production in the eastern tropical North Atlantic, *Biogeosciences*, 12, 7467-7482, 10.5194/bg-12-7467-2015, 2015.

Machu, E., Capet, X., Estrade, P. A., Ndoye, S., Brajard, J., Baurand, F., Auger, P.-A., Lazar, A., and Brehmer, P.: First Evidence of Anoxia and Nitrogen Loss in the Southern Canary Upwelling System, *Geophys. Res. Lett.*, 46, 2619-2627, 10.1029/2018gl079622, 2019.

McCoy, D., Bianchi, D., and Stewart, A. L.: Global observations of submesoscale coherent vortices in the ocean, *Prog. Oceanogr.*, 189, 102452, <https://doi.org/10.1016/j.pocean.2020.102452>, 2020.



McGillicuddy, D. J.: Formation of Intrathermocline Lenses by Eddy-Wind Interaction, *J. Phys. Oceanogr.*, 45, 606-612, 10.1175/jpo-d-14-0221.1, 2015.

McGillicuddy, D. J.: Mechanisms of Physical-Biological-Biogeochemical Interaction at the Oceanic Mesoscale, in: *Annual Review of Marine Science*, Vol 8, edited by: Carlson, C. A., and Giovannoni, S. J., *Annual Review of Marine Science*, Annual Reviews, Palo Alto, 125-+, 2016.

McWilliams, J. C.: Submesoscale, coherent vortices in the ocean, *Reviews of Geophysics*, 23, 165-182, 10.1029/RG023i002p00165, 1985.

Molemaker, M. J., McWilliams, J. C., and Dewar, W. K.: Submesoscale Instability and Generation of Mesoscale Anticyclones near a Separation of the California Undercurrent, *J. Phys. Oceanogr.*, 45, 613-629, 10.1175/jpo-d-13-0225.1, 2015.

Nof, D.: On the β -Induced Movement of Isolated Baroclinic Eddies, *J. Phys. Oceanogr.*, 11, 1662-1672, 10.1175/1520-0485(1981)011<1662:Otimoi>2.0.Co;2, 1981.

Peña-Izquierdo, J., van Sebille, E., Pelegrí, J. L., Sprintall, J., Mason, E., Llanillo, P. J., & Machín, F. (2015). Water mass pathways to the North Atlantic oxygen minimum zone. *Journal of Geophysical Research: Oceans*.

Philander, S. G. H.: Forced oceanic waves, *Reviews of Geophysics*, 16, 15-46, 10.1029/RG016i001p00015, 1978.

Reagan, James R.; Boyer, Tim P.; García, Hernán E.; Locarnini, Ricardo A.; Baranova, Olga K.; Bouchard, Courtney; Cross, Scott L.; Mishonov, Alexey V.; Paver, Christopher R.; Seidov, Dan; Wang, Zhankun; Dukhovskoy, Dmitry: *World Ocean Atlas 2023*. NOAA National Centers for Environmental Information, 2024

Rubino, A., Dotsenko, S., and Brandt, P.: Nonstationary Westward Translation of Nonlinear Frontal Warm-Core Eddies, *J. Phys. Oceanogr.*, 39, 1486-1494, 10.1175/2008jpo4089.1, 2009.

Schmidtko, S., Johnson, G. C., and Lyman, J. M.: MIMOC: A global monthly isopycnal upper-ocean climatology with mixed layers, *J. Geophys. Res.-Oceans*, 118, 1658-1672, 10.1002/jgrc.20122, 2013.

Schütte, F., Brandt, P., & Karstensen, J. (2016a). Occurrence and characteristics of mesoscale eddies in the tropical northeastern Atlantic Ocean. *Ocean Sci.*, 12(3), 663-685. <https://www.ocean-sci.net/12/663/2016/>, 2016

Schütte, F., Karstensen, J., Krahmann, G., Hauss, H., Fiedler, B., Brandt, P., Visbeck, M., and Körtzinger, A.: Characterization of "dead-zone" eddies in the eastern tropical North Atlantic, *Biogeosciences*, 13, 5865-5881, 10.5194/bg-13-5865-2016, 2016b.

Shcherbina, A. Y., Rudnick, D. L., and Talley, L. D.: Ice-draft profiling from bottom-mounted ADCP data, *J. Atmos. Ocean. Technol.*, 22, 1249-1266, 10.1175/jtech1776.1, 2005.

Stramma, L., Bange, H. W., Czeschel, R., Lorenzo, A., and Frank, M.: On the role of mesoscale eddies for the biological productivity and biogeochemistry in the eastern tropical Pacific Ocean off Peru, *Biogeosciences*, 10, 7293-7306, 10.5194/bg-10-7293-2013, 2013.

R. Srinivasan, V. Rajendran, Shijo Zacharia, Tata Sudhakar, M.A. Atmanand: Indigenized Indian Drifting Buoys with INSAT Communication for Ocean Observations, *Ocean Engineering*, Volume 145, 2017, <https://doi.org/10.1016/j.oceaneng.2017.08.054>.



Thomsen, S., Kanzow, T., Krahmann, G., Greatbatch, R. J., Dengler, M., and Lavik, G.: The formation of a subsurface anticyclonic eddy in the Peru-Chile Undercurrent and its impact on the near-coastal salinity, oxygen, and nutrient distributions, *Journal of Geophysical Research: Oceans*, 121, 476-501, doi:10.1002/2015JC010878, 2016.

van Leeuwen, P. J.: The Propagation Mechanism of a Vortex on the β Plane, *J. Phys. Oceanogr.*, 37, 2316-2330, 10.1175/jpo3107.1, 2007.

Vic, C., B. Ferron, V. Thierry, H. Mercier, and P. Lherminier, 2021: Tidal and Near-Inertial Internal Waves over the Reykjanes Ridge. *J. Phys. Oceanogr.*, 51, 419–437, <https://doi.org/10.1175/JPO-D-20-0097.1>.

Vic, C., & Ferron, B. (2023). Observed structure of an internal tide beam over the Mid-Atlantic Ridge. *Journal of Geophysical Research: Oceans*, 128, e2022JC019509. <https://doi.org/10.1029/2022JC019509>

Visbeck, M.: Deep velocity profiling using lowered acoustic Doppler current profilers: Bottom track and inverse solutions, *J. Atmos. Ocean. Technol.*, 19, 794-807, 10.1175/1520-0426(2002)019<0794:dvpu>2.0.co;2, 2002.



Table 1. Low-DO events (below $60 \mu\text{mol kg}^{-1}$) found in the upper 200 m during meridional CTD-O ship sections along 23°W between 7° and 12°N . Only those low-DO events are listed, where meridional sections of DO, hydrography and velocity were available (spanning a latitude range of minimum 3°). Columns from left to right denote DO minimum between 0 and 200 m, corresponding depth, latitude and research cruise with date of the CTD-O profile. The last three columns denote type, core position and radius of related eddy, that was analyzed with the eddy identification method. ACE events are marked in bold (the abbreviation ACME stands for anticyclonic mode water eddy). As an example, the event in the third row (Meteor 119/1, 17-Sep-2015) is presented in Fig. 4.

DO minimum [$\mu\text{mol kg}^{-1}$]	Depth [m]	Latitude [$^\circ\text{N}$]	Cruise ID (Date)	Eddy type	Eddy core position	Radius [km]
17	59	8,0	Meteor 116/1 (22-May-2015)	ACME	8.3 $^\circ\text{N}$ 23.1 $^\circ\text{W}$	33
37	63	11,5	Meteor 116/1 (21-May-2015)	-	-	-
42	71	8,0	Meteor 119/1 (17-Sep-2015)	ACME	8.0 $^\circ\text{N}$ 23.3 $^\circ\text{W}$	38
44	45	10,0	Ronald H. Brown PNE09 (24-Jul-2009)	ACME	10.3 $^\circ\text{N}$ 23.2 $^\circ\text{W}$	36
47	69	10,5	Polarstern PS88.2 (08-Nov-2014)	ACE	10.3 $^\circ\text{N}$ 23.2 $^\circ\text{W}$	37
48	77	11,5	Ronald H. Brown PNE09 (24-Jul-2009)	ACME	11.6 $^\circ\text{N}$ 22.9 $^\circ\text{W}$	31
52	75	11,5	L'Atalante IFM-GEOMAR 4 (11-Mar-2008)	-	-	-
53	67	11,0	Meteor 097/1 (30-May-2013)	-	-	-
54	93	7,0	Meteor 068/2 (04-Jul-2006)	ACME	7.1 $^\circ\text{N}$ 23.0 $^\circ\text{W}$	20
55	65	10,5	Merian 018/3 (25-Jun-2011)	-	-	-
56	74	7,0	Ronald H. Brown PNE06 (30-Jun-2006)	ACME	7.0 $^\circ\text{N}$ 23.0 $^\circ\text{W}$	45
57	71	11,5	Meteor 130/1 (03-Sep-2016)	-	-	-
58	82	11,0	Meteor 105/1 (10-Apr-2014)	ACME	11.0 $^\circ\text{N}$ 23.2 $^\circ\text{W}$	60
58	73	11,5	Merian 022/1 (15-Nov-2012)	ACME	11.6 $^\circ\text{N}$ 23.0 $^\circ\text{W}$	37
58	79	10,5	Meteor 106/1 (24-Apr-2014)	ACME	10.4 $^\circ\text{N}$ 23.2 $^\circ\text{W}$	33